Science and Technology for the Built Environment, (2020) **26**, 816–834

ISSN: 2374-4731 print / 2374-474X online
DOI: 10.1080/23744731.2020.1730661

Taylor & Francis
Taylor & Francis Group

Characterization of a thermal aerosol generator for HVAC filtration experiments (RP-1734)

TIANREN WU[1,2] AND BRANDON E. BOOR[1,2]*

[1]*Lyles School of Civil Engineering, Purdue University, 550 Stadium Mall Drive, West Lafayette, IN, 47907, USA*
[2]*Ray W. Herrick Laboratories, Center for High Performance Buildings, Purdue University, 177 South Russell Street, West Lafayette, IN, 47907, USA*

HVAC filters are exposed to a diverse mixture of aerosols during their service life. Aerosol physiochemical properties can have a significant impact on the removal efficiency and loading behavior of a filter. New aerosol generation techniques are needed to age HVAC filters with particle size distributions (PSDs) representative of those found in outdoor (urban) and indoor environments. This study evaluated the physical characteristics of salt aerosol produced by a newly designed commercially available thermal aerosol generator. The thermal aerosol generator produced a high mass output of sub-micron ($\leq$ 1,000 nm) sodium chloride (NaCl) and potassium chloride (KCl) particles by burning a salt stick in an oxygen-propane flame. The shape of the number and mass PSDs is similar to those found in outdoor (urban) and indoor air and can be modulated by varying the rate at which the salt stick is fed into the flame. The morphology of the NaCl and KCl particles varied with size, with compact spherical or cubic structures observed below 100 nm and agglomerates observed above 100 nm. The thermal aerosol generator is a cost-effective technique for rapid ageing of HVAC filters with a PSD that more accurately represents, compared to conventional loading dusts, what filters encounter in real HVAC installations.

Introduction

HVAC filters used in commercial and residential buildings encounter a complex mixture of aerosols of outdoor and indoor origin during their service life. Aerosols can span in size from a few nanometers to tens of micrometers (Seinfeld and Pandis 2012). Outdoor and indoor aerosols exhibit diverse characteristics, including morphological features, such as their particle size distribution (PSD), shape, and density; chemical and biological composition; whether they exist as a liquid, solid, or a phase state between the two; their tendency to uptake moisture (hygroscopicity); and the electrostatic charge that they carry (number of charges, polarity) (Pöschl 2005). These properties influence the size-resolved particle removal efficiency and dust loading behavior of HVAC filters (Poon and Liu 1997; Endo, Chen, and Pui 1998; Thomas et al. 1999, 2001; Valmari, Lehtimäki, and Taipale 2006; Wang and Otani 2012; Wang 2013; Wang and Tronville 2014; Montgomery, Green, and Rogak 2015; Abdolghader et al. 2018). As aerosols are captured by HVAC filters, they will begin to form complex deposits of solid dendrites and liquid films within the filter fiber matrix (Kasper, Schollmeier, and Meyer 2010; Barros, Tanabe, and Aguiar 2016; Gac et al. 2016). A combination of depth filtration and cake formation across the filter restricts airflow and imposes a pressure drop that must be overcome by the blower in the air handling unit (AHU) (Stephens, Novoselac, and Siegel 2010; Zaatari, Novoselac, and Siegel 2014; He et al. 2016). It is necessary to characterize the loading kinetics of HVAC filters aged with an aerosol representative of that found in outdoor (urban) and indoor environments in order to better predict the trend in airflow resistance, and associated AHU blower power draw to overcome this pressure drop, during a filter's service life.

Loading aerosols typically used to age HVAC filters include ISO-12103-1-A2 Fine Test Dust, ISO-12103-1-A4 Coarse Test Dust, and ASHRAE Test Dust per ANSI/ASHRAE Standard 52.2-2017 (Tronville and Rivers 2005; ASHRAE 2017). Such aerosols are primarily composed of coarse mode particles (1,000 to 100,000 nm). While useful for providing insights into differences in loading kinetics among filter media, coarse mode loading aerosols have a particle number and mass PSD unlike that found in outdoor (urban) and indoor environments (Hussein et al. 2004; Tronville and Rivers 2005; Seinfeld and Pandis 2012; Azimi, Zhao, and Stephens 2014; Stephens 2018; Fazli, Zeng, and Stephens 2019). Thus, the HVAC filter will

Received November 26, 2019; Accepted January 21, 2020
Tianren Wu, is a PhD Student. **Brandon E. Boor, PhD,** ASHRAE Associate Member, is an Assistant Professor.
This article has been republished with minor changes. These changes do not impact the academic content of the article.
*Corresponding author e-mail: bboor@purdue.edu

undergo a much different loading process than what it will encounter in real HVAC installations (Tronville and Rivers 2005, 2006; Valmari, Lehtimäki, and Taipale 2006).

Outdoor (urban) and indoor aerosol number PSDs are often dominated by particles smaller than 100 nm size, while mass PSDs include significant contributions from both the accumulation mode (100 to 2,500 nm) and a fraction of the coarse mode (2,500 to 10,000 nm) (Hussein et al. 2004; Tronville and Rivers 2005; Seinfeld and Pandis 2012; Azimi, Zhao, and Stephens 2014; Stephens 2018; Fazli, Zeng, and Stephens 2019). From the perspective of HVAC filter loading, it is of primary interest to reproduce outdoor (urban) and indoor aerosol mass PSDs as loading data is often expressed on a gravimetric basis (loaded particle mass per unit filter area). Filters aged with sub-micron particles ($\leq$1,000 nm) obtain significantly higher pressure drops at a given loaded mass compared to those aged with coarse mode particles (Poon and Liu 1997; Valmari, Lehtimäki, and Taipale 2006; He et al. 2016). It is expected that the evolution in the pressure drop of filters installed in commercial and residential AHUs will differ from loading curves obtained from coarse mode test dust.

Cost-effective, high mass output ($\geq$ 10 g/h) aerosol generators are needed to more accurately reproduce sub-micron mass PSDs of outdoor (urban) and indoor aerosols during HVAC filter loading experiments in full-scale experimental test facilities. Doing so will enable for a more realistic simulation of how filters are aged in real environments. Such generators are to be used in the proposed ASHRAE Guideline 35: Method for Determining the Energy Consumption Caused by Air-Cleaning and Filtration Devices. ASHRAE Guideline 35 will establish a consistent experimental methodology to determine the AHU blower energy consumption induced by HVAC filters as they are loaded with a sub-micron aerosol with a mass PSD representative of that found in actual HVAC systems in commercial buildings located in urban areas.

Numerous aerosol generation techniques are capable of producing sub-micron particles, including evaporation-condensation of metallic and organic vapors in tube furnaces, soot generation via diffusion flames, atomization of salts, spark-discharge generation, glowing hot-wire generation, electrospray generation, cold plasma via dielectric barrier discharge, and nanopowder dispersion (Biskos et al. 2008 and references therein). While such generation techniques can produce sub-micron aerosols with varied PSDs and other physiochemical properties, their mass production rates are often insufficient ($\leq$ 1 g/h) for conducting rapid ($\leq$ 8 hours) HVAC filter loading experiments as will be required in the proposed ASHRAE Guideline 35. One viable technique is thermal aerosol generation in which high mass concentrations of sub-micron salt particles are generated via evaporation-condensation of salt vapor (Edwards and Kinnear 1974; Vijayakumar and Whitby 1984; Zhang and Jiang 2016). Thermal aerosol generators can produce mass PSDs with mass median diameters of approximately 200 to 400 nm, however, characteristics of the salt aerosol have not yet been systematically assessed (Edwards and Kinnear 1974; Zhang and Jiang 2016).

The objective of this study is to evaluate the number and mass PSDs and morphological features of sodium chloride (NaCl) and potassium chloride (KCl) particles produced by a newly designed commercially available thermal aerosol generator under different operational conditions. The results will inform the suitability of such a generation technique for reproducing the sub-micron fraction of outdoor (urban) and indoor aerosol mass PSDs at high mass production rates for rapid HVAC loading experiments as per the proposed ASHRAE Guideline 35.

Materials and methods

Thermal aerosol generator

The thermal aerosol generator (Series 6000, SFP Services Ltd., Christchurch, UK) produces salt particles via evaporation-condensation by burning salt sticks in a high temperature oxygen-propane flame (Figure 1). The generator consists of a conventional blowtorch fitted with an annular burner, a battery-powered feeder for the salt stick, and two rotameters for controlling the flow rates of oxygen (O_2) and propane (C_3H_8). The O_2 and C_3H_8 flows are premixed and then ignited. A flame cone is formed in front of the annular burner. The salt stick passes through the nozzle of the annular burner from the rear and then enters the flame. The stick is gripped between a serrated drive roller connected to a variable speed motor and a smooth idler roller that is mounted on a sprung guide arm. The arm guide is fully opened when inserting the salt stick and then gently released to prevent damaging the salt stick prior to burning. The salt stick feed rate is calibrated by the manufacturer and can be controlled through a dial. The nominal flow rates of O_2 and C_3H_8 for generating the salt particles are 17 L/min and 4 L/min, respectively. The primary content of the salt sticks is NaCl or KCl, with a trace amount of magnesium oxide (MgO) added to serve as a binding agent for the stick. The MgO will not vaporize in the flame and will fall as hot ash. For each batch of salt sticks, the effective content (abundance of NaCl or KCl) is provided as a mass per unit length of the stick by the manufacturer. The effective content of the salt sticks analyzed in this study ranged from 99 to 144 mg/mm.

Experimental design

In this study, the number ($1/cm^3$) and mass ($\mu g/m^3$) PSDs of the salt aerosol synthesized by the thermal aerosol generator at different operational conditions were examined. Three operational factors were considered: the type of salt (NaCl and KCl), the feed rate of the salt stick (3, 5, 10, 18, and 25 mm/min), and the diameter of the stick (10 and 12 mm). Salt particles were generated for both salt types at each feed rate and for both stick diameters, thus a total of twenty operating conditions were examined. During the experiments, the thermal aerosol generator was placed in a fume hood. The duration of each PSD experiment varied with the feed rate. For tests with a feed rate of 3, 5, and 10 mm/min, the test duration was 20 to 30 minutes. For tests with a feed rate of 18 and 25 mm/min, the test duration was 15 to 20 minutes

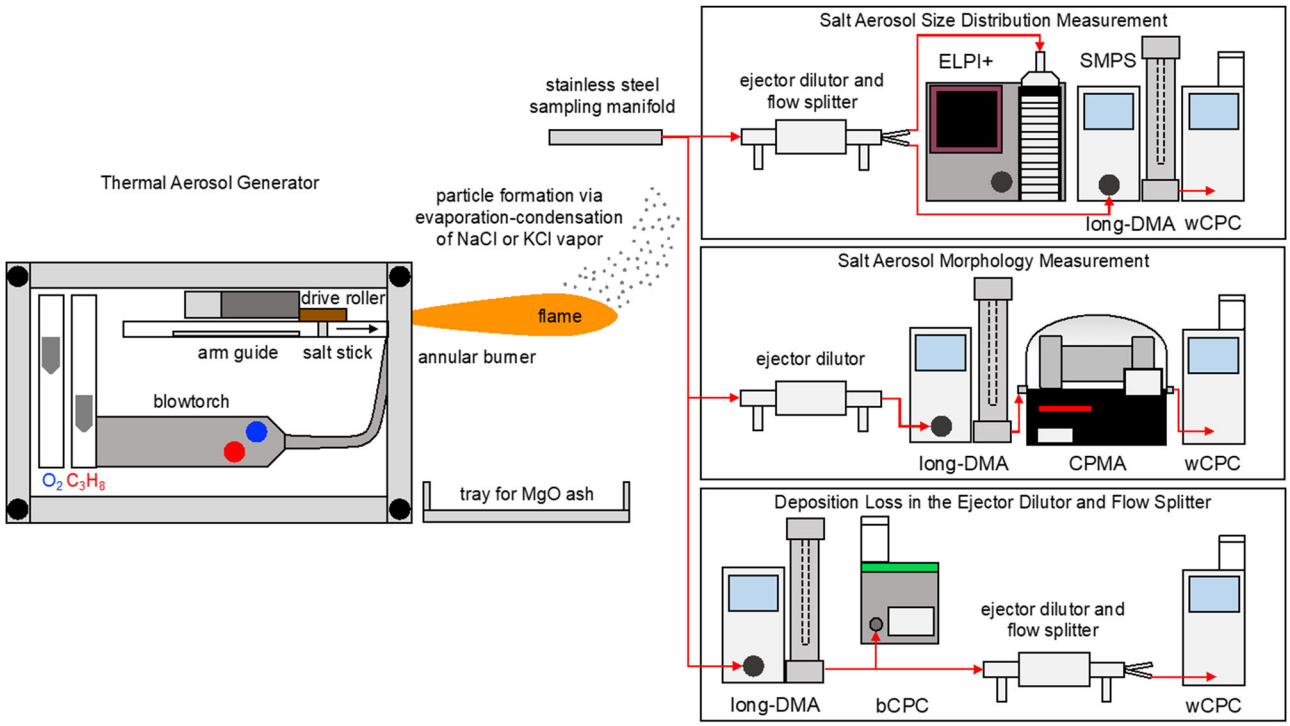

Figure 1. Setup for thermal aerosol generator experiments: (top) measurement of salt aerosol particle size distributions, (middle) measurement of salt aerosol morphological features, and (bottom) evaluation of particle deposition loss in the ejector dilutor and flow splitter assembly.

due to the high consumption rate of the salt sticks. Morphological features of the salt particles were characterized in a sub-set of experiments for 10 mm sticks of both salt types at a feed rate of 5 mm/min.

Measurement of salt aerosol size distributions

The salt aerosol was extracted at 50 cm above the flame of the thermal generator via a stainless steel sampling manifold. The aerosol sample was diluted by an ejector dilutor (DI-1000, Dekati Ltd., Kangasala, Finland) and then entered a flow splitter (Model 1104, Brechtel Manufacturing Inc., Hayward, CA, USA) prior to measurement of the PSD. A differential pressure gauge monitored the pressure difference between the inlet and outlet of the ejector dilutor, which was used to estimate the dilution factor according to the calibration curve provided by the manufacturer. Electrical mobility diameter (D_{em})-based number PSDs of the salt aerosol were measured with a Scanning Mobility Particle Sizer (SMPS, Model 3938NL88, TSI Inc., Shoreview, MN, USA), consisting of a Kr-85 bi-polar charger (370 MBq, Model 3077 A, TSI Inc., Shoreview, MN, USA), a long Differential Mobility Analyzer (long-DMA, Model 3081, TSI Inc., Shoreview, MN, USA), and a water-based Condensation Particle Counter (wCPC, Model 3788, TSI Inc., Shoreview, MN, USA). Aerodynamic diameter (D_a)-based number PSDs were measured with a High Resolution Electrical Low-Pressure Impactor (HR-ELPI+, Dekati Ltd., Kangasala, Finland). Sintered collection plates were used to eliminate particle bounce and impactor overloading. The HR-ELPI + was operated in normal resolution mode with fourteen size fractions from 6 to 10,000 nm in D_a (henceforth referred to as ELPI+).

Measurement of salt aerosol morphological features

Morphological features of the NaCl and KCl particles, including size-resolved effective densities (ρ_{eff}), size-resolved dynamic shape factors (χ), and mass-mobility exponents (ε_m), were determined by combining a long-DMA with a Centrifugal Particle Mass Analyzer (CPMA, Cambustion Ltd., Cambridge, UK) and a wCPC (Figure 1). The DMA-CPMA-CPC technique is used to evaluate the mass-mobility relationship of an aerosol population (Olfert and Collings 2005). Here, the effective density (ρ_{eff}) is defined as the ratio of the particle mass (m_p) to the volume assuming a sphere with a diameter of D_{em} (Equation 1, DeCarlo et al. 2004). The dynamic shape factor (χ) is defined as the ratio of the actual drag force on the particle to the drag force on a sphere with a diameter equal to the volume equivalent diameter (D_{ve}) (Hinds 2012). χ is used to characterize the irregular, non-spherical shape of the particle (Hinds 2012). χ is unity for a sphere, often greater than 1 for an irregular particle, and can approach and exceed 2 for agglomerates (DeCarlo et al. 2004; Mikhailov et al. 2004). The mass-mobility exponent (ε_m) is used to describe the fractal nature of the particles. ε_m approaches 3 for a sphere and becomes less than 2 for fractal agglomerates formed by diffusion-limited processes. The combination of ρ_{eff}, χ, and ε_m enable for a quantitative assessment of the morphology of the NaCl

and KCl particles produced by the thermal generator. Such parameters are useful in interpreting number and mass PSDs and in understanding how the morphological features of the salt aerosol may impact the filtration mechanisms and loading behavior of HVAC filters.

As with the PSD measurements, the salt aerosol was extracted at 50 cm above the flame and diluted with an ejector dilutor. The aerosol sample passed through a Kr-85 bi-polar charger to achieve a Boltzmann equilibrium charge distribution. The salt particles then entered the long-DMA, which operated in stepping mode to select particles with a certain D_{em}. The sample and sheath flow rates of the long-DMA were set at 1.5 L/min and 7.5 L/min, respectively.

Following mobility classification with the long-DMA, the particles were further classified by their mass-to-charge ratio with the CPMA. As the particles pass through the gap between the inner and outer coaxial rotating electrodes of the CPMA, they experience opposing centrifugal and electrostatic forces. Particles can penetrate the CPMA only when the two forces are in balance. By adjusting the rotation speed and the voltage potential between the inner and outer electrodes, the mass-to-charge setpoint can be controlled, thereby selecting particles with a certain mass. At each D_{em} setpoint, the CPMA scanned over a wide mass range with a fixed mass resolution ($R_m = 5$). At the downstream location of the CPMA, a wCPC measured the number concentration of the mobility- and mass-classified particles. The concentration at each mass setpoint was averaged over 4 seconds with a delay of 3 seconds between two measurement points.

The DMA-CPMA-CPC measurements were used to estimate variations in the ρ_{eff} for a given D_{em}, termed the ρ_{eff} distribution, through the following equation (DeCarlo et al. 2004):

$$\rho_{eff} = \frac{6m_p}{\pi D_{em}^3} \quad (1)$$

Many of the ρ_{eff} distributions presented a dominant peak and a shoulder (Figure 2), the latter of which is due to doubly-charged particles. Thus, each ρ_{eff} distribution was fitted with two normal distributions that represent the singly- and doubly-charged particles, respectively. The mean ρ_{eff} of the fitting for the singly-charged particles was adopted as the ρ_{eff} for a given D_{em} setpoint, and the standard deviation was adopted as the uncertainty of the measurement. Thus, size-resolved effective density functions, ρ_{eff} (D_{em}), were determined for both NaCl and KCl.

An example fitting of a ρ_{eff} distribution for a D_{em} setpoint of 121 nm is illustrated in Figure 2. The red circles represent the measured data points. The dark blue dashed line on the left represents the singly-charged particles with a nominal diameter of 121 nm, while the light blue dashed line on the right represents the doubly-charged particles with a nominal diameter of 186.3 nm. This fitting method is used simply to differentiate the singly- and doubly-charged particles and does not take the transfer functions of the DMA and CPMA into consideration. Therefore, the width of the reported ρ_{eff} distribution is relatively wide compared to the actual distribution, which can be obtained by a data

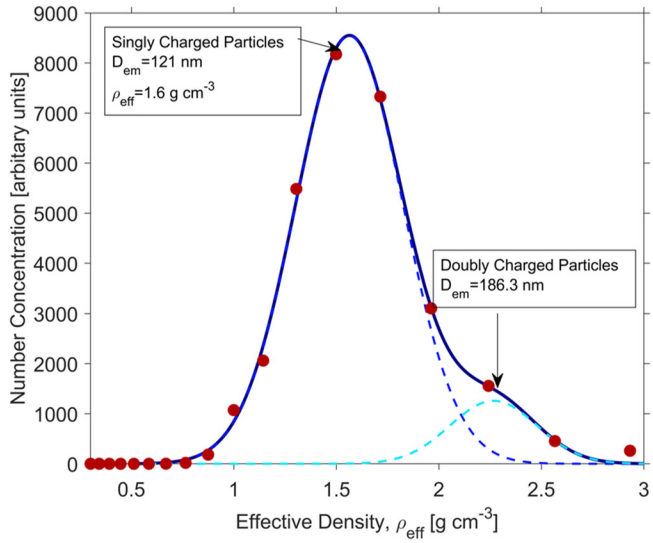

Figure 2. An example of the two-mode fitting for the effective density (ρ_{eff}) distribution with a DMA setting of D_{em} = 121 nm. The red circles represent the measured data points via the DMA-CPMA-CPC setup. The two dashed lines represent the fitted ρ_{eff} distributions for the singly (dark blue) and doubly (light blue) charged particles. The solid blue line represents the sum of the two fitted ρ_{eff} distributions.

inversion routine that accounts for the charging efficiency of the bi-polar charger, transfer functions of the long-DMA and CPMA, and the wCPC detection efficiency (Buckley et al. 2017; Rawat et al. 2016). However, due to temporal fluctuations of the salt aerosol PSDs during the operation of the thermal aerosol generator, the inversion of the measured data was not successful.

Dynamic shape factors of the NaCl and KCl particles were estimated as a function of D_{em}. First, the D_{ve} corresponding to each D_{em} setpoint was calculated from the ρ_{eff} and the bulk density of the salt (ρ_m) via Equation (2), assuming no internal voids within the particles such that the bulk density and particle density (ρ_p) are equivalent (DeCarlo et al. 2004):

$$D_{ve} = \sqrt[3]{\frac{6m_p}{\pi\rho_m}} = \sqrt[3]{\frac{\rho_{eff} D_{em}^3}{\rho_m}} \quad (2)$$

The dynamic shape factor at a given D_{em} can be estimated by Equation (3), which defines the relationship between D_{em} and D_{ve} (DeCarlo et al. 2004):

$$\chi = \frac{D_{em}}{D_{ve}} \frac{C_c(D_{ve})}{C_c(D_{em})} \quad (3)$$

where C_c is the Cunningham Slip Correction Factor (Hinds 2012).

The mass-mobility exponent (ε_m) was determined for the NaCl and KCl particles to characterize their fractal-like nature. The mass-mobility relationship of particles formed via diffusion-limited processes, such as soot particles and metal agglomerates, can be described by a power law function (Park et al. 2003; Olfert, Symonds, and Collings 2007;

Shin et al. 2009; Pagels et al. 2009; Shin, Mulholland, and Pui 2010a; Eggersdorfer et al. 2012; Rissler et al. 2013; Leskinen et al. 2014; Charvet et al. 2014):

$$m_p = KD_{em}^{\varepsilon_m} \quad (4)$$

where K is a constant. Combining Equations (1) and (4), we obtain the following equation relating ρ_{eff}, D_{em}, and ε_m:

$$\rho_{eff} = \frac{6KD_{em}^{\varepsilon_m - 3}}{\pi} \quad (5)$$

The size-resolved effective density functions, ρ_{eff} (D_{em}), were fit with Equation (5) to estimate ε_m for each salt type.

Particle deposition loss in the ejector dilutor and flow splitter

The size-resolved particle deposition loss fraction in the dilutor-flow splitter assembly was measured by the setup shown in Figure 1. The salt particles were first mobility classified by the long-DMA. Particle number concentrations were then measured at the upstream and downstream locations of the dilutor-flow splitter assembly with a butanol-based CPC (bCPC, Model A20, Airmodus Ltd., Helsinki, Finland) and a wCPC, respectively. The deposition loss fraction for particles with a diameter i (L_i) can be calculated as:

$$L_i = 1 - \frac{C_{2,i} \times DF}{C_{1,i}} \quad (6)$$

where DF is the nominal dilution factor, which can be inferred by the difference in pressure between the inlet and outlet of the ejector dilutor; $C_{2,i}$ is the particle number concentration at the downstream location of the dilutor-flow splitter assembly; and $C_{1,i}$ is the particle number concentration at the upstream location of the dilutor-flow splitter assembly. The correction factor for the deposition loss of particles with a diameter i (α_i) in the assembly can be expressed as:

$$\alpha_i = \frac{1}{L_i} \quad (7)$$

The number PSDs of the salt particles as measured by the SMPS and ELPI + were corrected for particle deposition in the dilutor-flow splitter assembly using α_i and the tubing of the sampling manifold using empirical relationships, as described in the Supplemental Material (Gormley and Kennedy 1948; Pich 1972; Crane and Evans 1977; Kulkarni, Baron, and Willeke 2011). The corrected PSDs were then multiplied by the DF of the dilutor.

Analysis of salt aerosol size distributions

The number PSDs measured by the SMPS and ELPI + were reported as a function of D_{em} and D_a, respectively. Mass PSDs were only determined from the ELPI + measurements given the wider operational size range of the instrument, which covered the full accumulation mode (100 to 2,500 nm). To convert the measured number PSDs of the ELPI + to mass PSDs, the D_a impactor cutoffs for each stage of the ELPI + were first transformed to D_{em}. This was done as the relationship between particle mass and ρ_{eff} is defined through D_{em}, not D_a (Equation 1). To relate D_a to D_{em}, Equations (2) and (3) are combined to derive

$$\rho_{eff} = \frac{\rho_m}{\chi^3} \frac{C_c(D_{ve})^3}{C_c(D_{em})^3} \quad (8)$$

D_{ve} can be converted to D_a according to DeCarlo et al. (2004) and assuming no internal voids such that ρ_m and ρ_p are equivalent

$$D_a = D_{ve}\sqrt{\frac{1}{\chi}\frac{\rho_m}{\rho_0}\frac{C_c(D_{ve})}{C_c(D_a)}} \quad (9)$$

where ρ_0 is standard density (1 g/cm^3). Combining Equations (3) and (9), we can define the relationship between D_{em} and D_a:

$$\frac{D_a}{D_{em}} = \frac{1}{\chi^{3/2}}\sqrt{\frac{\rho_m}{\rho_0 C_c(D_a)}}\frac{C_c(D_{ve})^{3/2}}{C_c(D_{em})} \quad (10)$$

Substituting Equation (8) into Equation (10), D_a can be converted to D_{em} using ρ_{eff}:

$$\frac{\rho_{eff}}{\rho_0} = \left(\frac{D_a}{D_{em}}\right)^2 \frac{C_c(D_a)}{C_c(D_{em})} \quad (11)$$

After converting D_a to D_{em}, the number PSDs measured by the ELPI + were converted to D_{em}-based mass PSDs using ρ_{eff} (D_{em}) via Equation (1). The mean number and mass PSDs for each thermal generator operational condition were normalized by the maximum value in each PSD to better visualize the PSD shape and the prominent mode(s). The normalized PSDs were then fit to the multi-lognormal distribution function (Seinfeld and Pandis 2012). Time-series plots of the number and mass PSDs were used to characterize the stability of the thermal generator output.

Results and discussion

The following sections present the results of the experimental investigation into the characteristics of salt particles produced by the thermal aerosol generator. First, size-resolved morphological features of the NaCl and KCl particles are discussed. Number and mass size distributions are then presented, followed by mass production rates. The results explain how operational conditions of the thermal generator influence the physical properties of the synthesized aerosol, thereby informing the utility of such a generation technique for HVAC filter loading experiments as per ASHRAE Guideline 35.

Morphological features of salt aerosol produced by the thermal aerosol generator

Figure 3 presents the measured effective densities (ρ_{eff}) of the NaCl and KCl particles produced by the thermal generator as a function of electrical mobility diameter, D_{em}. The measured effective densities (denoted as markers) are compared with theoretical ρ_{eff} values calculated by Equation (8)

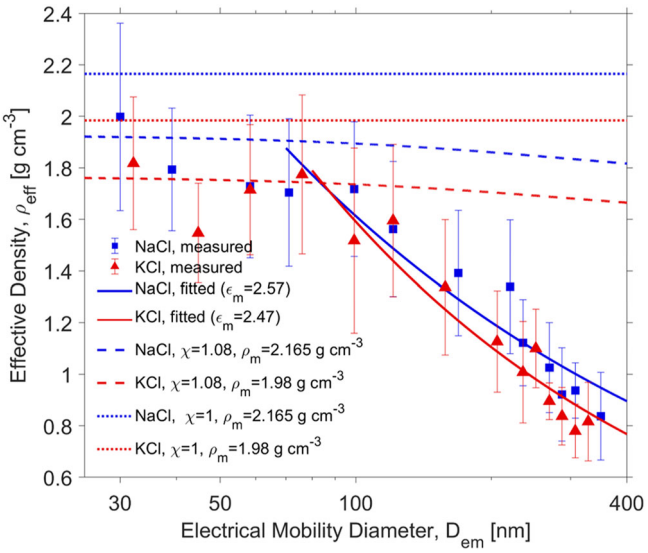

Figure 3. Measured size-resolved effective densities (ρ_{eff}) for NaCl (blue squares) and KCl (red triangles) particles. The error bars represent the standard deviation of the fitting for the ρ_{eff} distribution for resolving the singly and doubly charged particles for each D_{em}. Theoretical ρ_{eff} values calculated by Equation (8) using the bulk density of NaCl (ρ_m = 2.165 g/cm^3) and KCl (ρ_m = 1.98 g/cm^3) are shown assuming the particles adopt either a cubic structure (χ = 1.08, dashed lines) or spherical structure (χ = 1, dotted lines). The power law function (Equation 4) was fit to the measured ρ_{eff} data to determine the mass-mobility exponent (ε_m) for NaCl (solid blue line) and KCl (solid red line) particles.

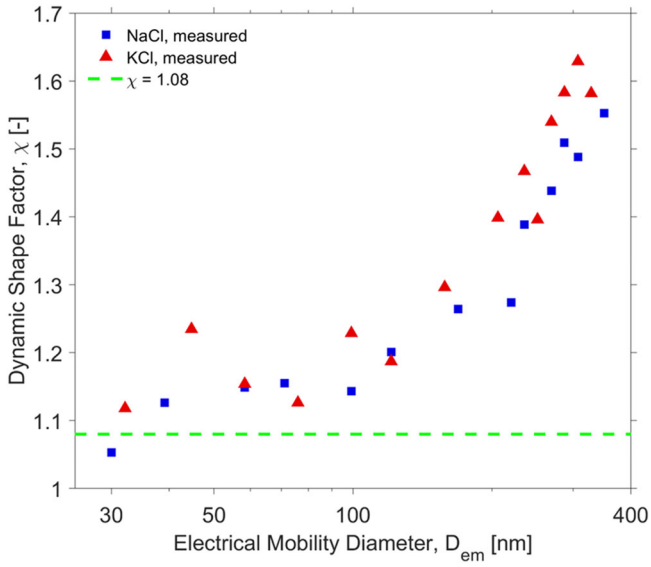

Figure 4. The measured size-resolved dynamic shape factors (χ) for NaCl (blue squares) and KCl (red triangles) particles. The χ for particles adopting a cubic structure (χ = 1.08) is provided as a reference (dashed green line).

using the bulk density of NaCl (ρ_m = 2.165 g/cm^3) and KCl (ρ_m = 1.98 g/cm^3) and assuming the particles adopt either a spherical (χ = 1, dotted lines) or cubic structure (χ = 1.08, dashed lines).

The effective densities of both NaCl and KCl particles varied with particle size. This size-dependency was most pronounced for D_{em} > 100 nm. For D_{em} < 100 nm, the salt aerosol was more morphologically consistent. Across the electrical mobility span of D_{em} = 30 to 100 nm, ρ_{eff} exhibited a small variation with particle size, with an average ρ_{eff} of 1.79 ± 0.11 g/cm^3 (mean ± SD) for NaCl particles and 1.67 ± 0.12 g/cm^3 for KCl particles. Between D_{em} = 100 and 400 nm, the effective densities for NaCl and KCl particles decreased with increasing particle size. For NaCl particles, ρ_{eff} decreased from 1.72 ± 0.26 at D_{em} = 99.2 nm to 0.84 ± 0.17 at D_{em} = 350 nm. For KCl particles, ρ_{eff} decreased from 1.52 ± 0.36 at D_{em} = 99.2 nm to 0.82 ± 0.15 at D_{em} = 328 nm.

The effective densities for each salt were nearest to their respective bulk densities at D_{em} = 30 nm for NaCl (ρ_{eff} = 2.00 ± 0.36 g/cm^3) and D_{em} = 32.1 nm for KCl (ρ_{eff} = 1.82 ± 0.26 g/cm^3). From D_{em} = 30 to 100 nm, the measured ρ_{eff} were within 8-23% of the theoretical ρ_{eff} calculated for spherical particles (χ = 1) with the bulk density of each salt. Above D_{em} = 100 nm, the measured ρ_{eff} deviated significantly from that for a sphere.

Intuitively, it may be assumed that NaCl and KCl particles adopt a cubic structure with a χ = 1.08 (for an ideal cube; Hinds (2012)) as the crystal structure of both salts are cubic. The cubic assumption results in theoretical ρ_{eff} values of approximately 1.7 to 1.9 g/cm^3 across the measured size range. The measured ρ_{eff} was closest to that for a cube for particles less than D_{em} = 80 nm. For particles larger than D_{em} = 100 nm, the measured ρ_{eff} was much less than that for a cube.

The morphologies of the NaCl and KCl particles synthesized by the thermal generator can be further interpreted through size-resolved dynamic shape factors (χ), which are presented in Figure 4. χ increased with particle size for both salt types from D_{em} = 30 to 400 nm. A sharp increase in χ was observed for particles larger than D_{em} = 100 nm. For NaCl particles, χ increased from 1.05 at D_{em} = 30 nm to 1.55 at D_{em} = 350 nm. Similarly, for KCl particles, χ increased from 1.12 at D_{em} = 32.1 nm to 1.58 at D_{em} = 328 nm. From D_{em} = 30 to 100 nm, the dynamic shape factors are similar to that for compact clusters of three (χ = 1.15) or four (χ = 1.17) spheres (Hinds (2012)).

NaCl and KCl particles exhibited similar trends in their size-resolved morphologies across the measured size range. Effective densities for KCl particles were generally 5 to 10% lower than that for the NaCl particles. Conversely, the dynamic shape factors for KCl particles were generally 2 to 9% greater than that of the NaCl particles.

The morphological features of the thermal generator aerosol can be compared with NaCl and KCl particles generated by other techniques. Zelenyuk, Cai, and Imre (2006) demonstrated that NaCl particles generated via nebulizing aqueous NaCl solutions could adopt three types of morphologies depending upon particle size and drying conditions,

including: nearly spherical ($\chi \sim 1.02$), cubic ($\chi \sim 1.065$ to 1.17), and agglomerates ($\chi \sim 1.3$ to 1.4). The effective densities of the spherical particles were found to be close to the bulk density of NaCl, while the effective densities of the agglomerates were between 1.2 to 1.4 g/m^2. Wang et al. (2010) found that the drying rate can influence χ while generating NaCl particles from aqueous solutions. For a given particle size, χ decreases with an increase in drying rate. NaCl particles formed by evaporation-condensation, as is the case for the thermal generator, tend to form agglomerates. Through electron microscopy, Craig and McIntosh (1952) revealed that chain-like cubic NaCl particles are formed through evaporation-condensation of NaCl in a tube furnace. Similarly, Krämer, Pöschl, and Niessner (2000) found NaCl agglomerates formed by evaporation-condensation to have a branched-chain structure with $\chi \sim 5$. In contrast to NaCl particles, there is comparatively less information on the morphology of KCl particles. Chindapan, Niamnuy, and Devahastin (2018) used scanning electron microscopy to show that KCl particles generated by a spray dryer have a highly agglomerated structure. The morphologies of KCl particles formed by evaporation-condensation have not been investigated to date in the literature.

The measured ρ_{eff} and χ, and their comparison with theoretical values and results from previous experimental studies, suggests that NaCl and KCl particles smaller than $D_{em} = 100$ nm adopt spherical or cubic structures or compact clusters thereof, while those larger than $D_{em} = 100$ nm adopt irregular morphologies suggestive of agglomerates. As particle size increases from $D_{em} = 100$ nm to 400 nm, the NaCl and KCl particles become progressively more chain-like and agglomerated with a decrease in ρ_{eff} and an increase in χ. However, electron microscopy analysis of the salt particles is needed to verify the results of the DMA-CPMA-CPC measurements.

The fractal-like nature of the NaCl and KCl agglomerates can be further characterized by the mass-mobility exponent (ε_m) in the power law function (Equation (4)), which describes the relationship between particle mass (m_p) and electrical mobility diameter (D_{em}). The power law function was fit to the measured effective density data from $D_{em} =$ 71.1 to 350 nm for NaCl and from $D_{em} = 76$ to 328 nm for KCl (solid lines in Figure 3). A coefficient of determination (R^2) of 0.89 and 0.92 for NaCl and KCl, respectively, indicates that the mass-mobility relationship for both salt types can be described well by the power law function.

The ε_m for NaCl and KCl were found to be 2.57 and 2.47, respectively. These values are within the range of mass-mobility exponents reported for agglomerates synthesized through different techniques, further demonstrating that the NaCl and KCl particles adopt an irregular, agglomerated structure beyond $D_{em} = 100$ nm. Previous studies indicate that the ε_m of soot particles generated from heavy-duty diesel engines, light-duty vehicles, premixed charge compression ignition combustion, and flame soot generators can vary from 2.2 to 2.56 (Park et al. 2003; Olfert, Symonds, and Collings 2007; Lo et al. 2009; Xue et al. 2009; Barone et al. 2011; Rissler et al. 2013). Leskinen et al. (2014) found the ε_m of particles generated from small-scale combustion of different solid wood fuels to be in the range of 2.22 to 2.46. Shin et al. (2010) reported a ε_m of 2.126 for silver agglomerates from $D_{em} = 80$ to 300 nm generated via evaporation-condensation of silver in a tube furnace. Charvet et al. (2014) used a spark discharge generator to generate metal agglomerates with constantan, copper, graphite, iron, silver, and titanium, and found ε_m for these agglomerates to be in the range from 1.98 to 2.329.

The size-resolved ρ_{eff} of NaCl and KCl particles generated by the thermal generator show a slightly different pattern from those measured in urban atmospheric environments. The average ρ_{eff} of NaCl and KCl particles between $D_{em} = 30$ to 100 nm are greater than those reported for urban aerosols in the same size range, which are typically between 1.14 to 1.58 g/cm^3 (Geller, Biswas, and Sioutas 2006; Levy et al. 2013; McMurry et al. 2002; Qiao et al. 2018; Xie et al. 2017; Yin et al. 2015). The average ρ_{eff} for NaCl and KCl particles in this size range are similar to that of H_2SO_4, $(NH_4)_2SO_4$, and NH_4NO_3 (approximately 1.7 to 1.83 g/cm^3), which are common inorganic components of urban aerosols (Lide 2004; Mikhailov et al. 2013; Neusüß et al. 2002; Tang 1996; Xiao et al. 2015). However, they are greater than those measured for organic aerosols and soot particles from vehicle exhaust (Barone et al. 2011; Kostenidou et al. 2007; Malloy et al. 2009; Maricq, Podsiadlik, and Chase 2000; Nakao et al. 2013; Zelenyuk et al. 2008).

NaCl and KCl particles between $D_{em} = 100$ to 220 nm exhibit ρ_{eff} values close to that reported for urban aerosols, while those greater than $D_{em} = 250$ nm present lower ρ_{eff} values compared to urban aerosols. The decrease in NaCl and KCl ρ_{eff} with increasing particle size is similar to the pattern observed for urban aerosol ρ_{eff} measured in near-traffic environments due to the existence of soot particles, which adopt a fractal-like morphology for $D_{em} > 100$ nm (Rissler et al. 2014). Geller, Biswas, and Sioutas (2006) found the urban aerosol ρ_{eff} measured at a freeway to be 1.13 g/cm^3 at $D_{em} = 50$ nm and 0.31 g/cm^3 at $D_{em} =$ 414 nm, with a mass-mobility exponent of 2.54, which is similar to the mass-mobility exponents of NaCl and KCl particles produced by the thermal generator.

A comparison of size-resolved ρ_{eff} of NaCl and KCl particles with those reported for indoor aerosols is constrained by the limited number of direct ρ_{eff} measurements for indoor aerosols. The ρ_{eff} of cigarette smoke can vary between 1.18 to 1.51 g/cm^3, which can be influenced by smoke mass, cigarette format, filter type, and mouth hold period (Johnson et al. 2014, 2015). It is suggested that the ρ_{eff} is independent of particle size, indicating that cigarette smoke particles likely adopt a spherical shape. The aerosol from secondhand smoke of waterpipe tobacco was reported to adopt a mass-mobility exponent of 2.85 with a ρ_{eff} of 1.25 g/cm^3 at $D_{em} = 80$ nm and 0.98 g/cm^3 at $D_{em} = 400$ nm (Markowicz et al. 2014). The ρ_{eff} of several indoor aerosol sources were calculated by Vu et al. (2017). Vacuum cleaning, kitchen cleaning, and tobacco smoking were found to generate aerosols with ρ_{eff} values of 1.16, 0.88, and 1.56 g/cm^3, respectively.

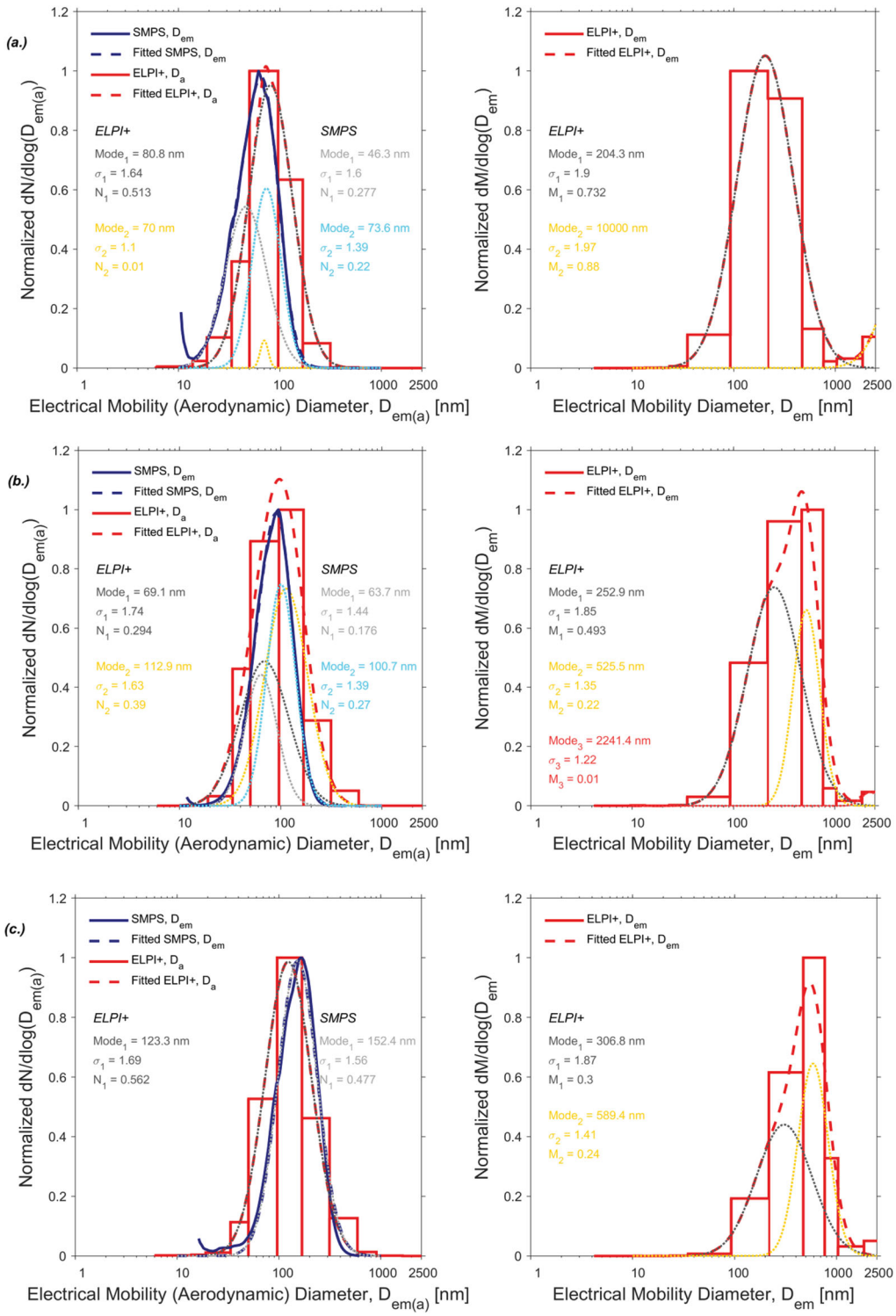

Figure 5. Normalized mean number (left) and mass (right) particle size distributions (PSDs) of NaCl particles generated by salt sticks with a diameter of 10 mm at feed rates of: (a.) 3 mm/min, (b.) 5 mm/min, (c.) 10 mm/min, and (d.) 18 mm/min. The solid blue lines represent the PSDs measured by the SMPS (number: D_{em}-based) and the red bar plots represent those measured by the ELPI+ (number: D_a-based, mass: D_{em}-based). The dashed lines represent the fitted multi-lognormal distribution functions (blue: SMPS, red: ELPI+) and the dotted lines represent the individual modes. The multi-lognormal distribution function parameters for each mode are listed on the side: $Mode_i$ = modal diameter (nm), σ_i = geometric standard deviation (–), and N_i or M_i = normalized number or mass amplitude, respectively (–). The NaCl PSDs for the feed rate of 25 mm/min are not presented since the salt stick clogged the nozzle of the thermal aerosol generation during the experiment.

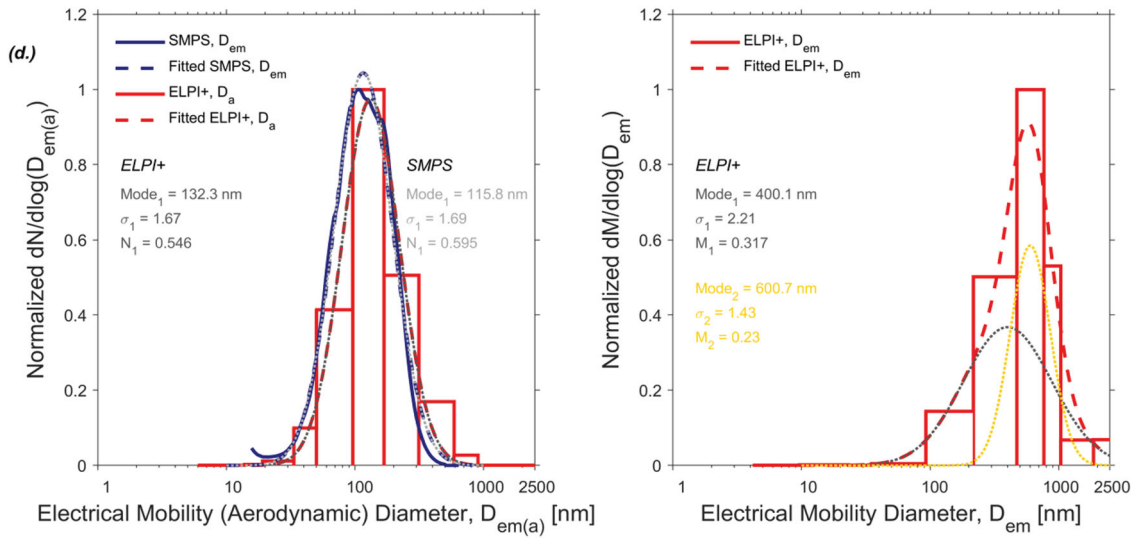

Figure 5. (Continued).

Number and mass size distributions of salt aerosol produced by the thermal aerosol generator

Figures 5–8 present the normalized mean number and mass PSDs of NaCl and KCl particles produced by the thermal aerosol generator for different salt stick feed rates (3, 5, 10, 18, and 25 mm/min) and diameters (10 and 12 mm). Number PSDs as measured by the SMPS (D_{em}-based) and ELPI+ (D_a-based) are presented, along with D_{em}-based mass PSDs estimated from the ELPI + number PSDs (D_a transformed to D_{em}) and size-resolved effective densities. The measured PSDs are fitted to the multi-lognormal distribution function and function parameters are included for each mode: $Mode_i$ = modal diameter (nm), σ_i = geometric standard deviation (–), and N_i or M_i = normalized number or mass amplitude, respectively (–).

The shape of the normalized mean number PSDs as measured by the SMPS (D_{em}-based) and ELPI+ (D_a-based) agree well across all experimental conditions. In general, the number PSDs for NaCl and KCl particles are unimodal and exhibit a single prominent peak in the sub-micron size fraction ($\leq$ 1,000 nm), with a significant number of particles in the ultrafine particle (UFP) size fraction ($\leq$ 100 nm). The shape of the NaCl and KCl number PSDs at a feed rate of 3 mm/min is similar to those reported in outdoor (urban) environments in European and North American cities, as well as number PSDs reported indoors under a variety of conditions (Hussein et al. 2004; Azimi, Zhao, and Stephens 2014; Stephens 2018; Fazli, Zeng, and Stephens 2019). The shape of the number PSDs at feed rates from 5 to 25 mm/min are similar to those reported in cities in China and India, where the number PSDs include a significant contribution from the accumulation mode (Mönkkönen et al. 2005; Peng et al. 2014). The width of the prominent peaks of the number PSDs is relatively narrow, with geometric standard deviations of individual modes often between 1.4 and 1.7. A partial secondary peak tends to appear below $D_{em} \sim$ 20 nm. This peak is unlikely to be associated with salt particles formed via evaporation-condensation, but rather particles formed by the O_2-C_3H_8 flame itself. The mixing ratio of the pre-mixed O_2-C_3H_8 is near, but does not reach, the fuel-lean condition. Particles in this secondary peak could include soot precursors or organic carbon. Previous studies suggest that under high temperature, small hydrocarbons (e.g. C_3H_8) can undergo a series of chemical reactions, including dehydrogenation, polymerization, cyclization, and radical chain reactions, to form larger polycyclic aromatic hydrocarbons (PAHs) or even soot nuclei within the flame (Frenklach 2002; Sgro et al. 2007, 2009; Wang 2011; Johansson et al. 2018).

The normalized mean mass PSDs are typically unimodal and present a dominant peak in the accumulation mode (100 to 2,500 nm) across all operating conditions of the thermal aerosol generator. The mass PSDs in the sub-micron fraction are representative of those found in outdoor (urban) and indoor environments (Tronville and Rivers 2005; Seinfeld and Pandis 2012; Azimi, Zhao, and Stephens 2014; Stephens 2018; Fazli, Zeng, and Stephens 2019). The mass PSDs tend to be wider compared to the number PSDs. This can be discerned through the geometric standard deviations of individual modes, which often exceed 1.7 for the mass PSDs. A partial secondary peak in the mass PSDs can be found at approximately 2,500 nm. This peak may be associated with residual MgO ash particles blown off the salt stick by the high-velocity O_2-C_3H_8 flow. Collection of the synthesized particles on filter substrates and subsequent electron microscopy analysis can verify the existence of the MgO ash particles.

The salt stick feed rate has the most significant influence on the shape of the PSDs among the three thermal aerosol generator operational factors that were evaluated (salt type, feed rate, and stick diameter). For both salt types and stick diameters, the prominent peaks of the number PSDs shift to larger particle sizes as the salt stick feed rate increases. For example, the diameter of the prominent peak of the normalized mean number PSDs of KCl particles generated by the

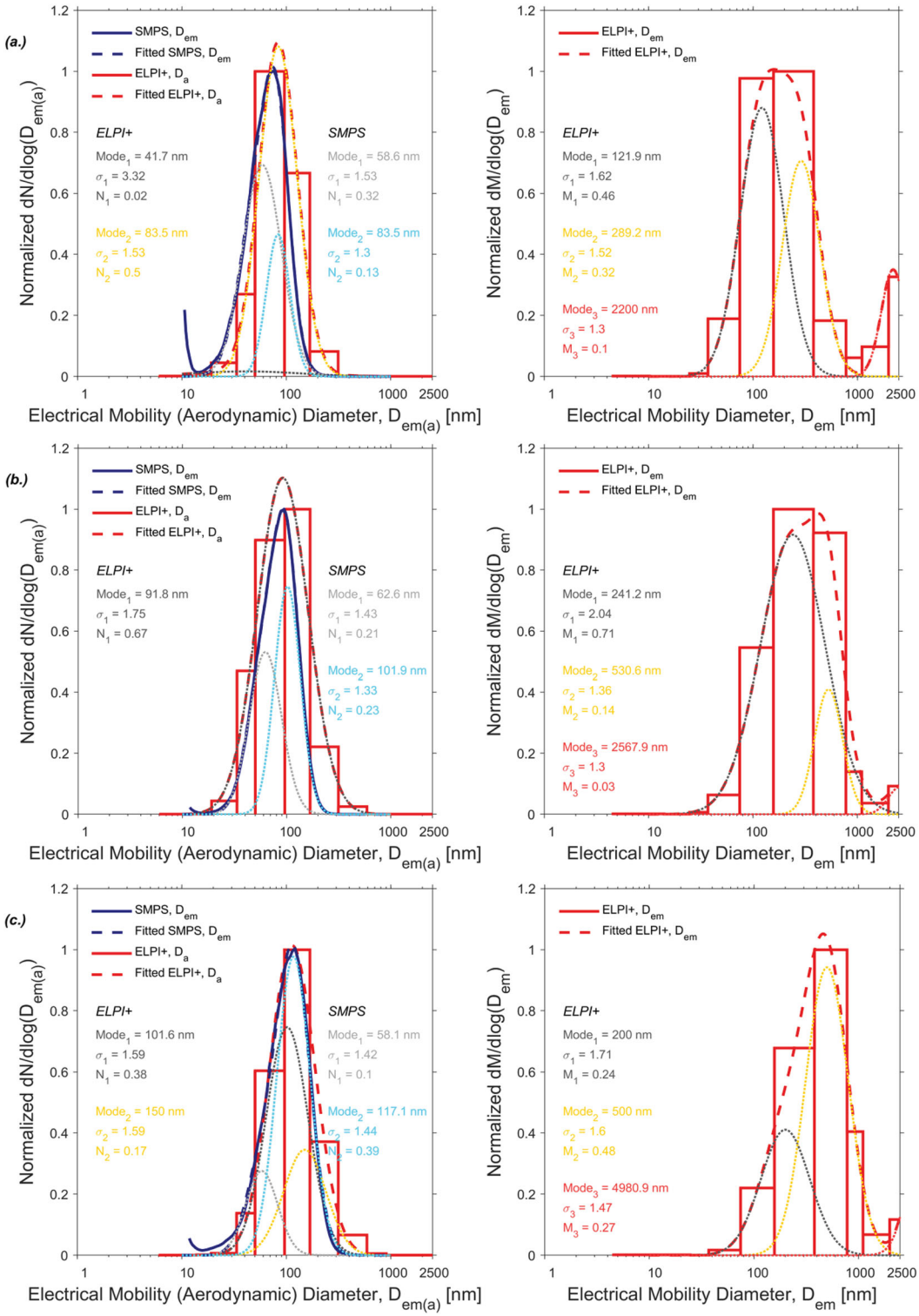

Figure 6. Normalized mean number (left) and mass (right) particle size distributions (PSDs) of KCl particles generated by salt sticks with a diameter of 10 mm at feed rates of: (a.) 3 mm/min, (b.) 5 mm/min, (c.) 10 mm/min, (d.) 18 mm/min, and (e.) 25 mm/min. The solid blue lines represent the PSDs measured by the SMPS (number: D_{em}-based) and the red bar plots represent those measured by the ELPI+ (number: D_a-based, mass: D_{em}-based). The dashed lines represent the fitted multi-lognormal distribution functions (blue: SMPS, red: ELPI+) and the dotted lines represent the individual modes. The multi-lognormal distribution function parameters for each mode are listed on the side: $Mode_i$ = modal diameter (nm), σ_i = geometric standard deviation (–), and N_i or M_i = normalized number or mass amplitude, respectively (–).

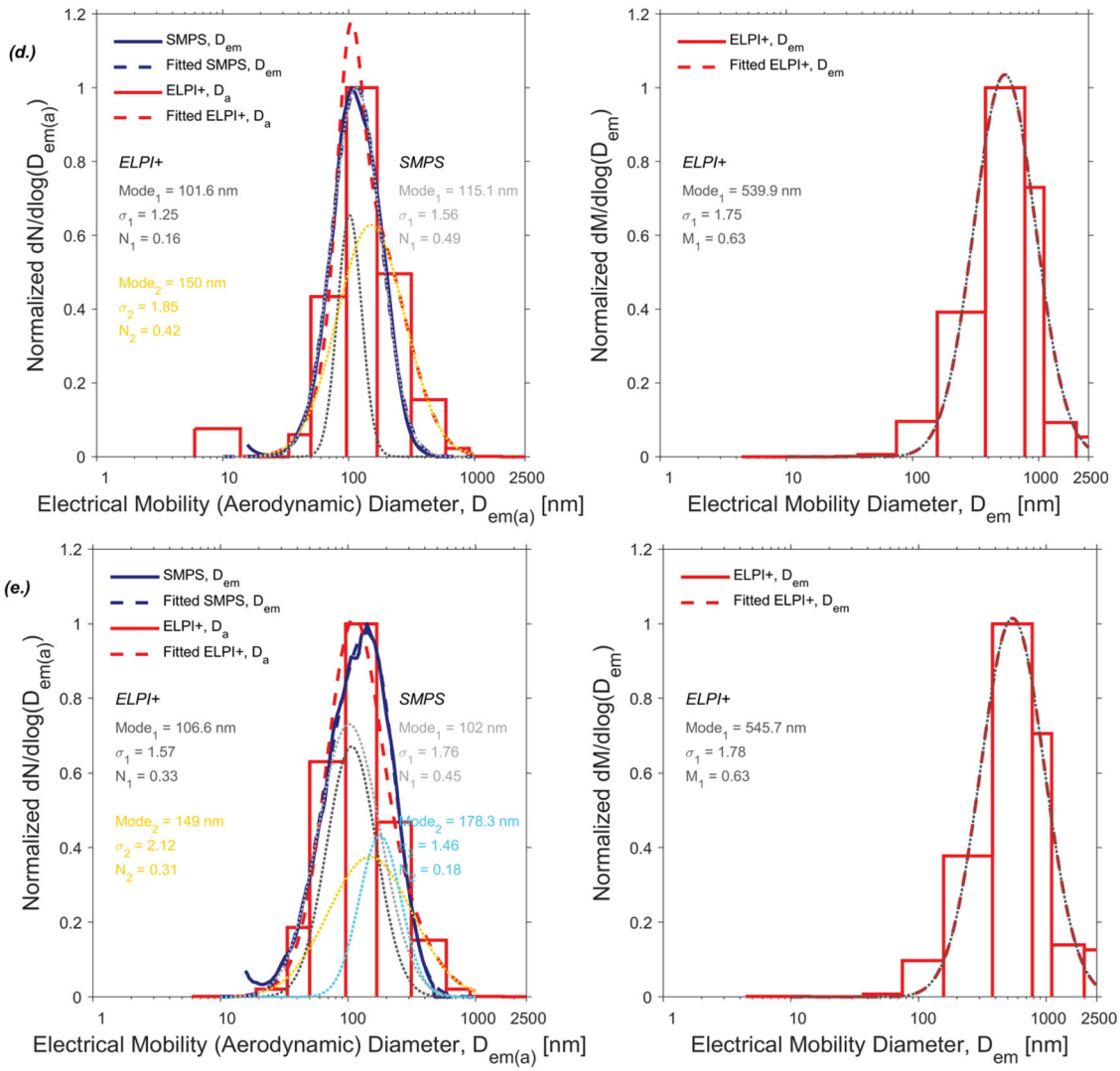

Figure 6. (Continued).

10 mm sticks is ~80 nm for a feed rate of 3 mm/min, ~90 nm for a feed rate of 5 mm/min, ~115 nm for feed rates of 10 and 18 mm/min, and ~140 nm for a feed rate of 25 mm/min (Figure 6). A gradual shift in the normalized mass PSDs with increasing feed rate is also observed for both salt types and stick diameters. For example, for KCl particles generated with 10 mm sticks, the prominent peak of the normalized mass PSDs shifts from ~200 nm to ~550 nm as the feed rate increases from 3 to 25 mm/min (Figure 6). The multi-lognormal fitting of each mass PSD demonstrates that the modal diameters of each individual mode also increase with the feed rate. The shift of the number and mass PSDs to larger particle size fractions with the increase in feed rate indicates that the salt particles are generally larger at higher feed rates. A possible explanation for this shift is that greater quantities of salt vapor are produced at higher feed rates which can aid condensational growth of the particles to larger sizes.

The shape of the number and mass PSD output of the thermal aerosol generator is not strongly influenced by the salt stick diameter and salt type. The 10 and 12 mm sticks produce similar normalized mean number and mass PSDs for both NaCl and KCl, with only small variations observed in the location of the prominent peak and the modal diameters of individual modes for a given feed rate. For the same salt stick diameter and feed rate, the normalized mean number PSDs of NaCl and KCl particles are very similar. However, the KCl mass PSDs exhibit a larger shift with increasing feed rate compared to the NaCl particles. For example, the prominent peak of the normalized mass PSDs for KCl particles (12 mm sticks) increases from ~170 nm at 3 mm/min to ~700 nm at 25 mm/min (Figure 8), whereas for NaCl (12 mm sticks), the peak increases from ~350 nm at 3 mm/min to ~590 nm at 25 mm/min (Figure 7).

The thermal aerosol generator produces a stable PSD output of sub-micron NaCl and KCl particles. Figure 9 shows example time-series plots of D_a-based number PSDs as measured by the ELPI + with a sampling interval of 1 second and D_{em}-based number PSDs as measured by the SMPS with a scan period of 70 seconds, both for NaCl particles generated by a salt stick with a diameter of 10 mm at a feed rate of 5 mm/min. The number PSDs are relatively stable

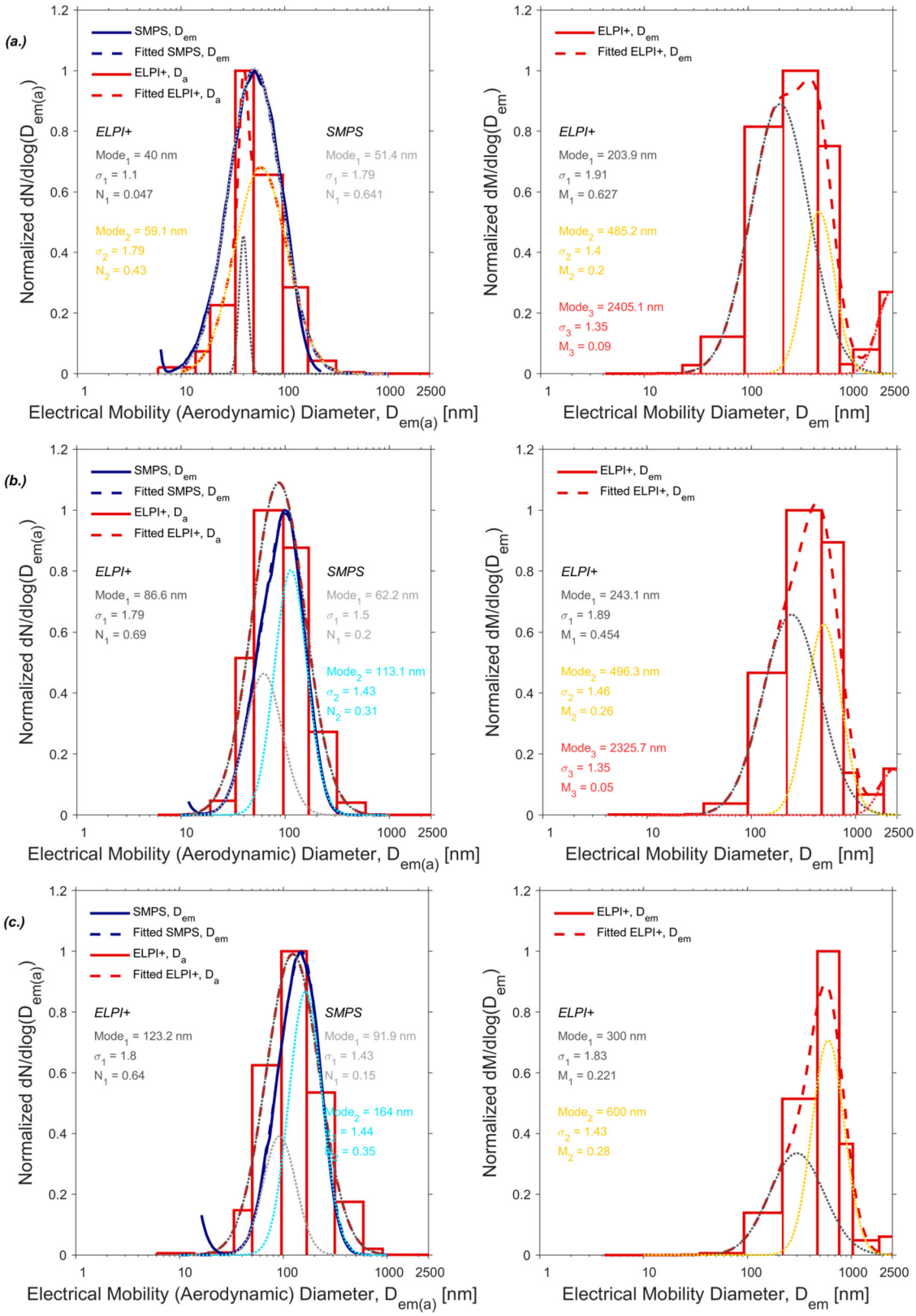

Figure 7. Normalized mean number (left) and mass (right) particle size distributions (PSDs) of NaCl particles generated by salt sticks with a diameter of 12 mm at feed rates of: (a.) 3 mm/min, (b.) 5 mm/min, (c.) 10 mm/min, (d.) 18 mm/min, and (e.) 25 mm/min. The solid blue lines represent the PSDs measured by the SMPS (number: D_{em}-based) and the red bar plots represent those measured by the ELPI+ (number: D_a-based, mass: D_{em}-based). The dashed lines represent the fitted multi-lognormal distribution functions (blue: SMPS, red: ELPI+) and the dotted lines represent the individual modes. The multi-lognormal distribution function parameters for each mode are listed on the side: $Mode_i$ = modal diameter (nm), σ_i = geometric standard deviation (–), and N_i or M_i = normalized number or mass amplitude, respectively (–).

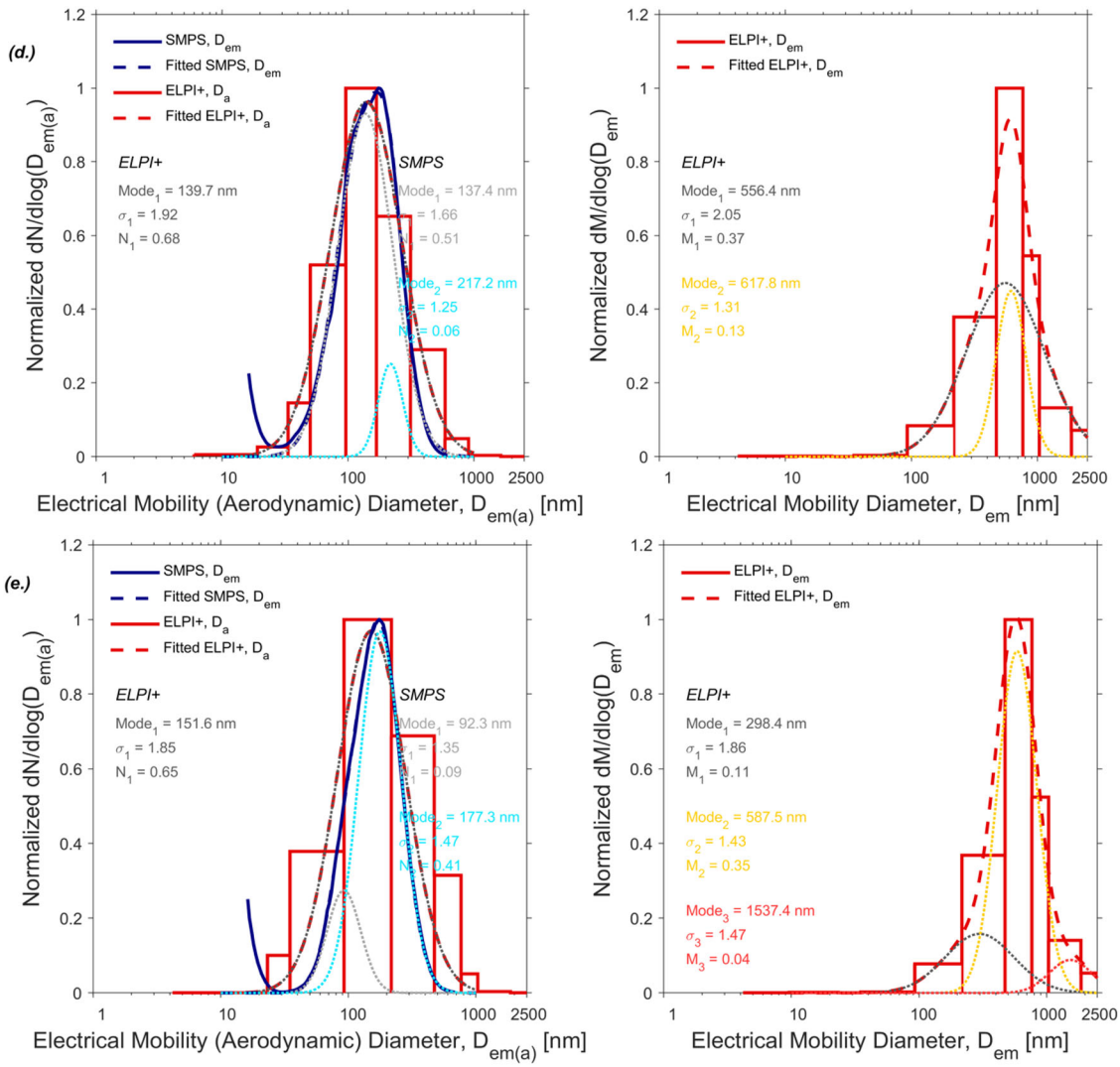

Figure 7. (Continued).

over the measurement period of 30 minutes. This is especially true for the PSD measurements made with the ELPI+. More pronounced temporal variations are observed in the SMPS measurements as an artifact of the longer scan period. A high concentration of NaCl particles can be found across the size range from ~30 to ~300 nm, which is consistent with the normalized mean number PSDs (Figure 5b). A clear peak is observed at ~100 nm in the number PSDs measured by both the ELPI + and SMPS.

Mass production rates of salt aerosol produced by the thermal aerosol generator

The thermal aerosol generator is intended to be used for HVAC filtration experiments to evaluate filter mass loading curves, defined as the relationship between the filter pressure drop and loaded particle mass per unit filter area. As such, the mass production rate of the thermal aerosol generator at different operational conditions is an important parameter to be characterized. Figure 10 presents estimated nominal mass production rates as the product of the salt stick feed rate and the effective content (salt mass per unit length), assuming the entirety of the salt is vaporized and condensed to form particles. Nominal mass production rates ranged from 18 to 207 g/h, depending on the salt type, feed rate, and stick diameter. The production rate is most sensitive to the feed rate.

The nominal mass production rates are likely to be overestimates of the actual production rates. The entirety of the salt mass may not get fully vaporized in the O_2-C_3H_8 flame and some of the non-vaporized salts may fall with MgO as ash. Actual production rates derived from the PSD measurements and a material balance model could not be determined due to uncertainties in characterization of the airflow regime within the fume hood where the thermal aerosol generator was housed. Delivery of the salt particles into a HVAC filtration test facility necessitates the design of a precisely controlled carrier flow system and evaluation of how the carrier flow system affects the transformation of the salt particles through coagulation and deposition. Such a system will enable accurate determination of the mass production rate.

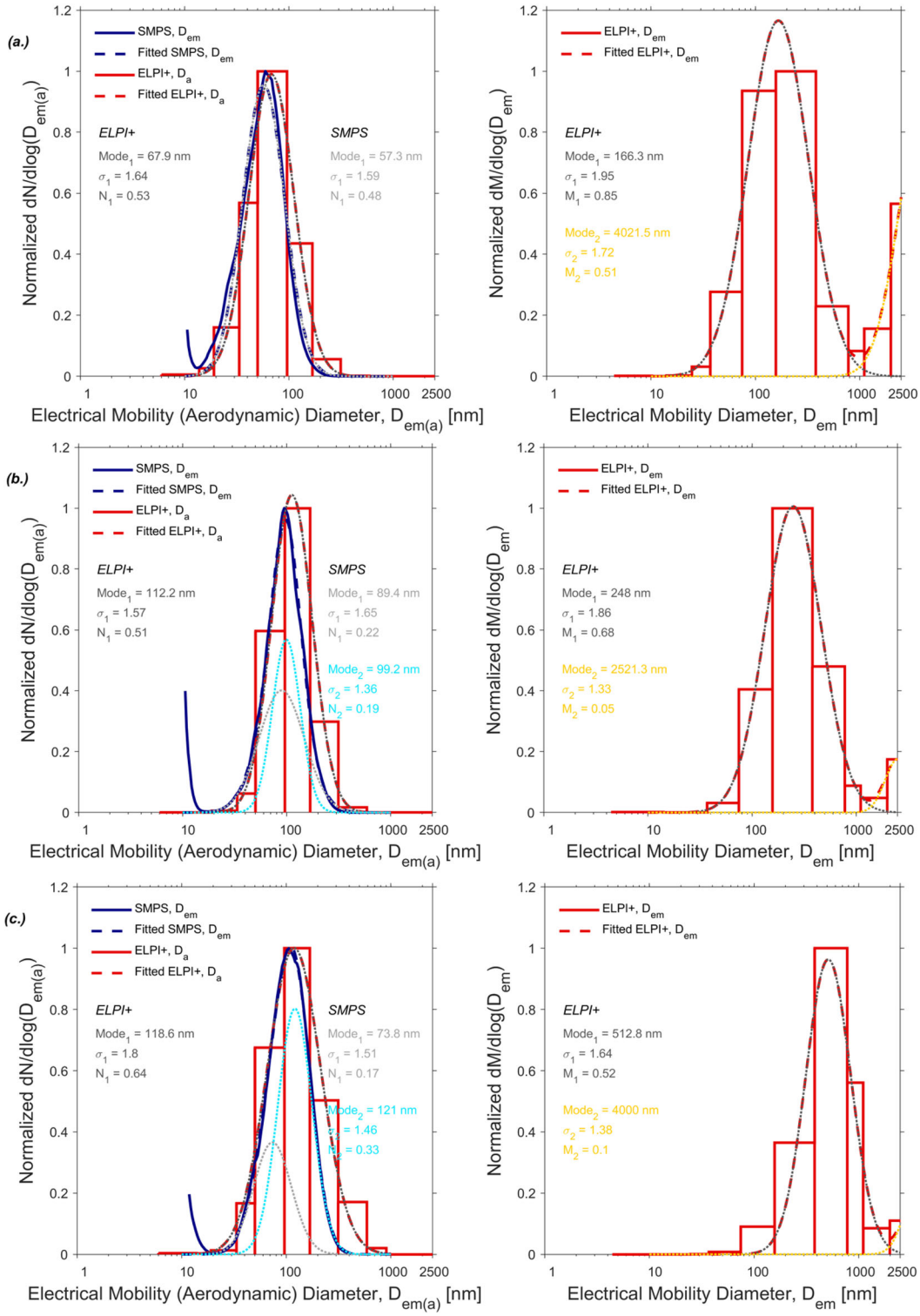

Figure 8. Normalized mean number (left) and mass (right) particle size distributions (PSDs) of KCl particles generated by salt sticks with a diameter of 12 mm at feed rates of: (a.) 3 mm/min, (b.) 5 mm/min, (c.) 10 mm/min, (d.) 18 mm/min, and (e.) 25 mm/min. The solid blue lines represent the PSDs measured by the SMPS (number: D_{em}-based) and the red bar plots represent those measured by the ELPI+ (number: D_a-based, mass: D_{em}-based). The dashed lines represent the fitted multi-lognormal distribution functions (blue: SMPS, red: ELPI+) and the dotted lines represent the individual modes. The multi-lognormal distribution function parameters for each mode are listed on the side: $Mode_i$ = modal diameter (nm), σ_i = geometric standard deviation (–), and N_i or M_i = normalized number or mass amplitude, respectively (–).

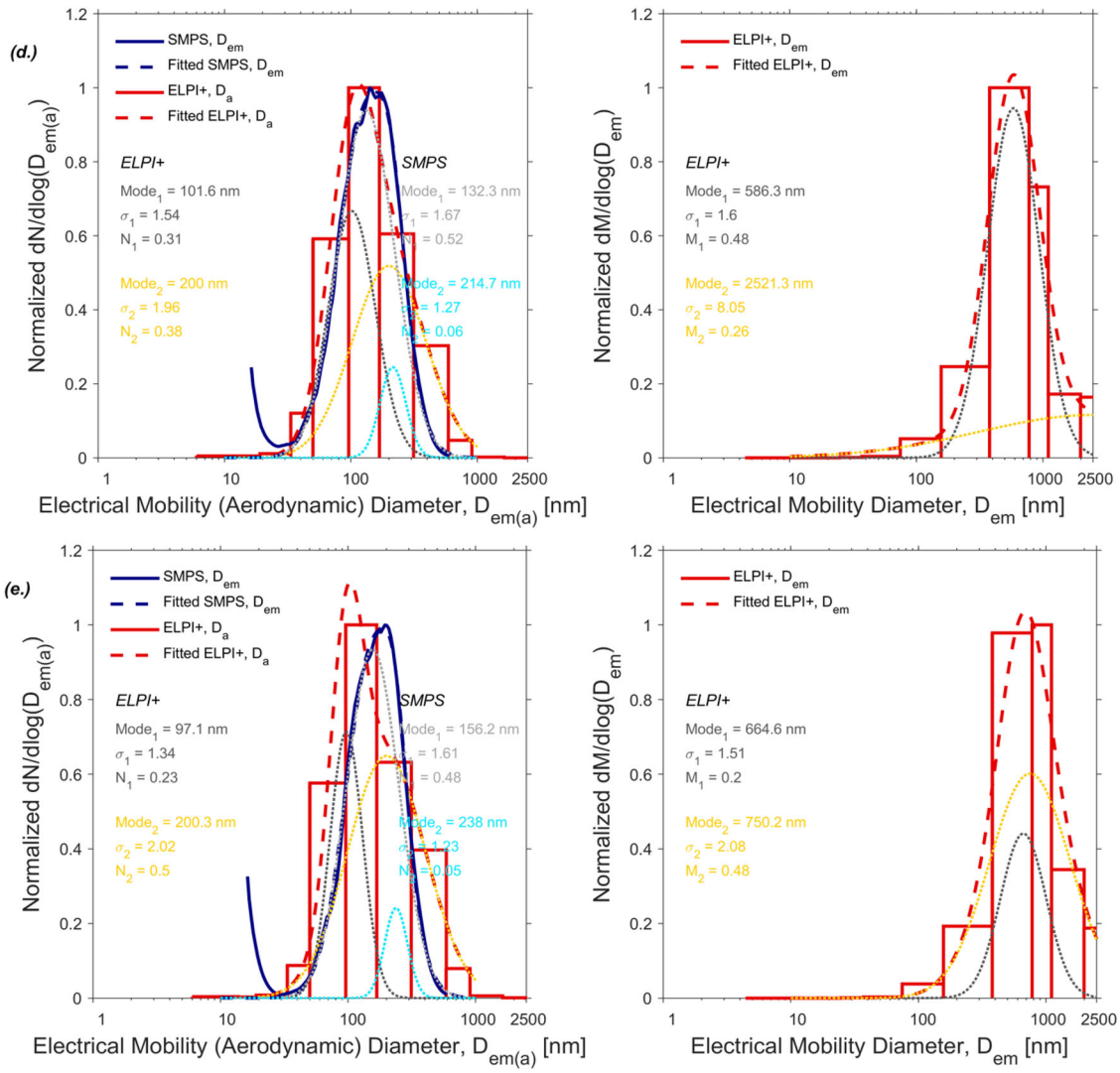

Figure 8. (Continued).

Measurement uncertainties due to unipolar and bi-polar charging of the salt aerosol

The morphological characterization of the salt aerosol demonstrated that NaCl and KCl particles larger than $D_{em} =$ 100 nm adopt irregular morphologies suggestive of agglomerates. This may induce uncertainties in the unipolar charging of the particles in the ELPI+ (via a unipolar corona charger) and bi-polar charging of the particles in the SMPS (via a Kr-85 bi-polar charger). The charging efficiency of the unipolar corona charger of the ELPI + was calibrated with particles of a compact morphology. Previous studies indicate that agglomerates can carry more charges per particle than a sphere with the same D_{em} when passing through a unipolar corona charger. Thus, the particle number concentration measured by the ELPI + may be overestimated. Shin et al. (2010b) found that the mean charge per particle for loose silver agglomerates is higher than that for coalesced spheres with the same D_{em} by 24% after unipolar corona charging. Ouf and Sillon (2009) suggested that the corona charger of the ELPI could induce a higher charging efficiency for fractal soot particles compared to compact spherical or cubic particles by up to 25%. Oh, Park, and Kim (2004) indicated that titanium dioxide agglomerates could have about 30% more charges than sintered spherical particles using an indirect photoelectric charger. During the thermal aerosol generator PSD measurements, the concentrations of salt particles in the accumulation mode were likely overestimated relative to the UFPs as the particles became more agglomerated with the increase in size (Figure 3). Conversely, the concentrations of salt particles in the accumulation mode as measured by the SMPS may be underestimated. The SMPS employs a Kr-85 bi-polar diffusion charger. Maricq (2008) found that the single positive and negative charging fraction of soot agglomerates is 15% and 10% lower, respectively, than oil droplets at a $D_{em} =$ 400 nm. Since the salt particles are very likely agglomerates in the accumulation mode, the SMPS may underestimate the particle concentration due to low charging efficiency.

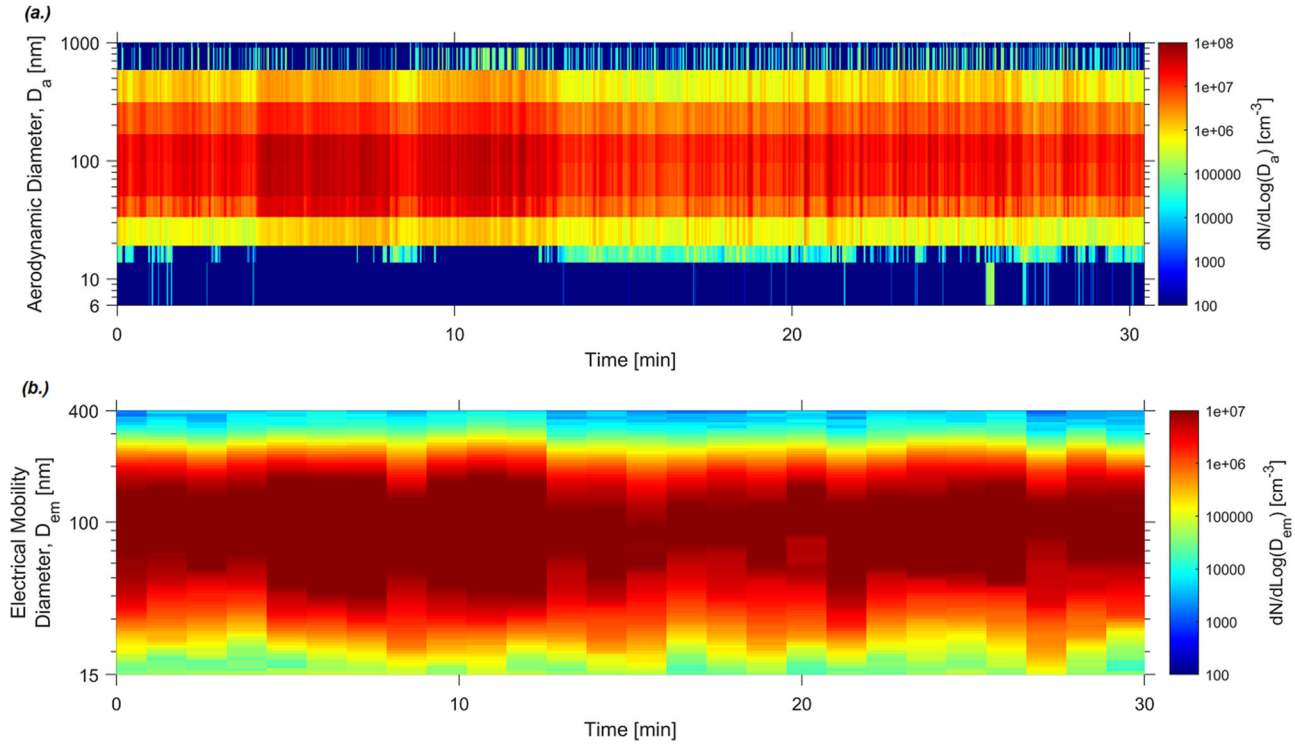

Figure 9. Time-series plots of (a.) D_a-based (ELPI+: sampling interval of 1 second) and (b.) D_{em}-based (SMPS: scan period of 70 seconds) number particle size distributions of NaCl particles generated by a salt stick with a diameter of 10 mm at a feed rate of 5 mm/min.

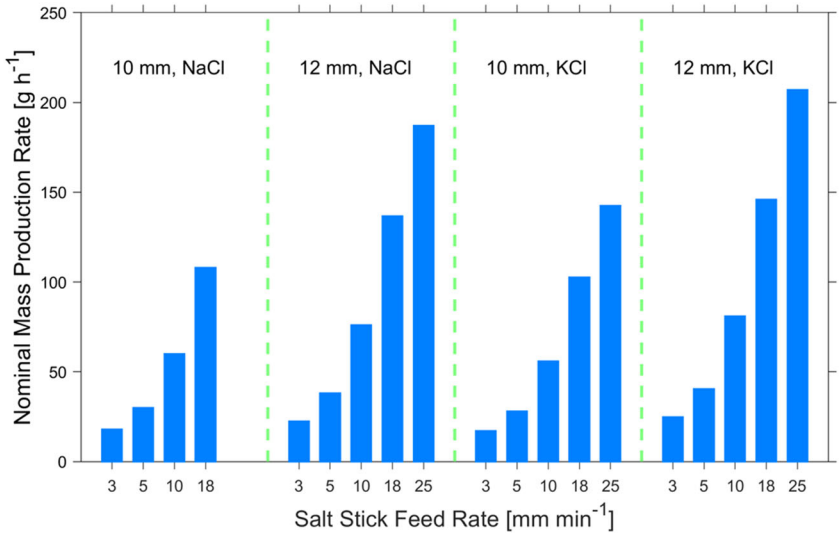

Figure 10. Nominal mass production rates of NaCl and KCl particles for both salt stick diameters (10 and 12 mm) as a function of the salt stick feed rate (3, 5, 10, 18, and 25 mm/min). The nominal mass production rates were calculated as the product of the salt stick feed rate and the effective content (salt mass per unit length), assuming the entirety of the salt is vaporized and condensed to form particles.

Conclusions

Physical characteristics of salt aerosol synthesized by a newly designed commercially available thermal aerosol generator under variable operational conditions were evaluated. The thermal aerosol generator produces a stable, high mass output of sub-micron NaCl and KCl particles by burning a stick of salt in an O_2-C_3H_8 flame. The generator is capable of creating salt aerosol with sub-micron number and mass PSDs similar in shape to those reported in outdoor (urban) and indoor environments. The salt stick feed rate has a pronounced impact on the PSD output, with increasing feed rate shifting the PSDs to larger sizes. The type of salt (NaCl, KCl) and salt stick diameter have a small influence on the

shape of the PSD. The feed rate can be varied from < 3 mm/min to 25 mm/min, providing a basis to modulate the PSD shape as per the requirements of the HVAC filtration experiment. The morphological features of the salt aerosol suggest that NaCl and KCl particles smaller than 100 nm adopt compact spherical or cubic structures, while those larger than 100 nm transition to agglomerates.

The detailed evaluation of the synthesized salt aerosol, including multi-lognormal distribution function parameters for number and mass PSDs, size-resolved effective densities and dynamic shape factors, and mass-mobility exponents provide a basis to understand how the aerosol characteristics can impact HVAC filtration performance during full-scale experiments. The thermal aerosol generator represents a cost-effective tool for rapid loading of HVAC filters with a sub-micron mass PSD similar to that found in real HVAC installations, and thus, is appropriate for use in the proposed ASHRAE Guideline 35 for evaluating the AHU blower energy implications of aged HVAC filters.

Acknowledgments

This work was supported by ASHRAE RP-1734. The authors are grateful for the support of the Project Monitoring Subcommittee: Paolo Tronville, Geoff Crosby, Bruce McDonald, Tom Justice, and Brian Krafthefer.

ORCID

Tianren Wu http://orcid.org/0000-0001-9214-3719
Brandon E. Boor http://orcid.org/0000-0003-1011-4100

References

Abdolghader, P., C. Brochot, F. Haghighat, and A. Bahloul. 2018. Airborne nanoparticles filtration performance of fibrous media: A review. *Science & Technology for the Built Environment* 24: 648–72. doi:10.1080/23744731.2018.1452454

ASHRAE 2017. *ANSI/ASHRAE Standard 52.2-2017: Method of testing general ventilation air-cleaning devices for removal efficiency by particle size*. Atlanta: American Society of Heating, Refrigerating and Air-Conditioning Engineers, Inc.

Azimi, P., D. Zhao, and B. Stephens. 2014. Estimates of HVAC filtration efficiency for fine and ultrafine particles of outdoor origin. *Atmospheric Environment* 98:337–46. doi:10.1016/j.atmosenv.2014.09.007

Barone, T. L., A. A. Lall, J. M. E. Storey, G. W. Mulholland, V. Y. Prikhodko, J. H. Frankland, J. E. Parks, and M. R. Zachariah. 2011. Size-resolved density measurements of particle emissions from an advanced combustion diesel engine: Effect of aggregate morphology. *Energy & Fuels* 25 (5):1978–88. doi:10.1021/ef200084k

Barros, P. M., E. H. Tanabe, and M. L. Aguiar. 2016. Performance of fibrous filters during nanoparticle cake formation. *Separation Science & Technology* 51 (6):1042–52. doi:10.1080/01496395.2015.1119845

Biskos, G., V. Vons, C. U. Yurteri, and A. Schmidt-Ott. 2008. Generation and sizing of particles for aerosol-based nanotechnology. *KONA Powder & Particle Journal* 26:13–35. doi:10.14356/kona.26.2008006

Buckley, D. T., S. Kimoto, M.-H. Lee, N. Fukushima, and C. J. Hogan. 2017. Technical note: A corrected two dimensional data inversion routine for tandem mobility-mass measurements. *Journal of Aerosol Science* 114:157–68. doi:10.1016/j.jaerosci.2017.09.012

Charvet, A., S. Bau, N. E. P. Coy, D. Bémer, and D. Thomas. 2014. Characterizing the effective density and primary particle diameter of airborne nanoparticles produced by spark discharge using mobility and mass measurements (tandem DMA/APM). *Journal of Nanoparticle Research* 16 (5):2418. doi:10.1007/s11051-014-2418-y

Chindapan, N., C. Niamnuy, and S. Devahastin. 2018. Physical properties, morphology and saltiness of salt particles as affected by spray drying conditions and potassium chloride substitution. *Powder Technology* 326:265–71. doi:10.1016/j.powtec.2017.12.014

Craig, A., and R. McIntosh. 1952. The preparation of sodium chloride of large specific surface. *Canadian Journal of Chemistry* 30 (5): 448–53. doi:10.1139/v52-053

Crane, R. I., and R. L. Evans. 1977. Inertial deposition of particles in a bent pipe. *Journal of Aerosol Science* 8 (3):161–70. doi:10.1016/0021-8502(77)90003-9

DeCarlo, P. F., J. G. Slowik, D. R. Worsnop, P. Davidovits, and J. L. Jimenez. 2004. Particle morphology and density characterization by combined mobility and aerodynamic diameter measurements. Part 1: Theory. *Aerosol Science & Technology* 38 (12):1185–205. doi:10.1080/027868290903907

Edwards, J., and D. I. Kinnear. 1974. Flame generation of sodium chloride aerosol for filter testing. Proceedings of the 13th AEC Air Cleaning Conference, San Francisco, August 12–15. 552–564.

Eggersdorfer, M. L., A. J. Gröhn, C. M. Sorensen, P. H. McMurry, and S. E. Pratsinis. 2012. Mass-mobility characterization of flame-made ZrO_2 aerosols: Primary particle diameter and extent of aggregation. *Journal of Colloid & Interface Science* 387 (1): 12–23. doi:10.1016/j.jcis.2012.07.078

Endo, Y., D.-R. Chen, and D. Y. H. Pui. 1998. Effects of particle polydispersity and shapefactor during dust cake loading on air filters. *Powder Technology* 98 (3):241–9. doi:10.1016/S0032-5910(98)00063-1

Fazli, T., Y. Zeng, and B. Stephens. 2019. Fine and ultrafine particle removal efficiency of new residential HVAC filters. *Indoor Air* 29 (4):656–69. doi:10.1111/ina.12566

Frenklach, M. 2002. Reaction mechanism of soot formation in flames. *Physical Chemistry Chemical Physics* 4 (11):2028–37. doi:10.1039/b110045a

Gac, J. M., A. Jackiewicz, Ł. Werner, and S. Jakubiak. 2016. Consecutive filtration of solid particles and droplets in fibrous filters. *Separation & Purification Technology* 170:234–40. doi:10.1016/j.seppur.2016.06.057

Geller, M., S. Biswas, and C. Sioutas. 2006. Determination of particle effective density in urban environments with a differential mobility analyzer and aerosol particle mass analyzer. *Aerosol Science & Technology* 40 (9):709–23. doi:10.1080/02786820600803925

Gormley, P. G., and M. Kennedy. 1948. Diffusion from a stream flowing through a cylindrical tube. *Proceedings of the Royal Irish Academy. Section A: Mathematical & Physical Sciences*, 52: 163–169.

He, X., B. T. Brem, Y. K. Bahk, Y.-Y. Kuo, and J. Wang. 2016. Effects of relative humidity and particle type on the performance and service life of automobile cabin air filters. *Aerosol Science & Technology* 50 (6):542–54. doi:10.1080/02786826.2016.1167832

Hinds, W. C. 2012. *Aerosol technology: Properties, behavior, and measurement of airborne particles*. Hoboken: John Wiley & Sons.

Hussein, T., A. Puustinen, P. P. Aalto, J. M. Mäkelä, K. Hämeri, and M. Kulmala. 2004. Urban aerosol number size distributions. *Atmospheric Chemistry & Physics* 4:391–411. doi:10.5194/acp-4-391-2004

Johansson, K. O., M. P. Head-Gordon, P. E. Schrader, K. R. Wilson, and H. A. Michelsen. 2018. Resonance-stabilized hydrocarbon-radical chain reactions may explain soot inception and growth. *Science* 361 (6406):997–1000. doi:10.1126/science.aat3417

Johnson, T. J., J. S. Olfert, R. Cabot, C. Treacy, C. U. Yurteri, C. Dickens, J. McAughey, and J. P. R. Symonds. 2014. Steady-state measurement of the effective particle density of cigarette smoke. *Journal of Aerosol Science* 75:9–16. doi:10.1016/j.jaerosci.2014.04.006

Johnson, T. J., J. S. Olfert, R. Cabot, C. Treacy, C. U. Yurteri, C. Dickens, J. McAughey, and J. P. R. Symonds. 2015. Transient measurement of the effective particle density of cigarette smoke. *Journal of Aerosol Science* 87:63–74. doi:10.1016/j.jaerosci.2015.05.006

Kasper, G., S. Schollmeier, and J. Meyer. 2010. Structure and density of deposits formed on filter fibers by inertial particle deposition and bounce. *Journal of Aerosol Science* 41 (12):1167–82. doi:10.1016/j.jaerosci.2010.08.006

Kostenidou, E., S. N. Pandis, R. K. Pathak, S. N. Pandis, E. Kostenidou, and S. N. Pandis. 2007. An algorithm for the calculation of secondary organic aerosol density combining ams and smps data. *Aerosol Science & Technology* 41 (11):1002–10. doi:10.1080/02786820701666270

Krämer, L., U. Pöschl, and R. Niessner. 2000. Microstructural rearrangement of sodium chloride condensation aerosol particles on interaction with water vapor. *Journal of Aerosol Science* 31 (6):673–85. doi:10.1016/S0021-8502(99)00551-0

Kulkarni, P., P. A. Baron, and K. Willeke. 2011. *Aerosol measurement: Principles, techniques, and applications*. Hoboken: John Wiley & Sons.

Leskinen, J., M. Ihalainen, T. Torvela, M. Kortelainen, H. Lamberg, P. Tiitta, G. Jakobi, J. Grigonyte, J. Joutsensaari, O. Sippula, et al. 2014. Effective density and morphology of particles emitted from small-scale combustion of various wood fuels. *Environmental Science & Technology* 48 (22):13298–306. doi:10.1021/es502214a

Levy, M. E., R. Zhang, A. F. Khalizov, J. Zheng, D. R. Collins, C. R. Glen, Y. Wang, X. Y. Yu, W. Luke, J. T. Jayne, et al. 2013. Measurements of submicron aerosols in Houston, Texas during the 2009 SHARP field campaign. *Journal of Geophysical Research: Atmospheres* 118 (18):10518–34.

Lide, D. R. 2004. *CRC Handbook of chemistry and physics.* Vol. 85. Washington: CRC Press.

Lo, J., A. Massling, E. Swietlicki, E. Vaclavik, M. Ketzel, J. Pagels, S. Loft, and E. Swietlicki. 2009. Experimentally determined human respiratory tract deposition of airborne particles at a busy street experimentally determined human respiratory tract deposition of airborne particles at a busy street. *Environmental Science & Technology* 43 (13):4659–64. doi:10.1021/es803029b

Malloy, Q. G. J., S. Nakao, L. Qi, R. Austin, C. Stothers, H. Hagino, and D. R. Cocker. 2009. Real-time aerosol density determination utilizing a modified scanning mobility particle sizer aerosol particle mass analyzer system. *Aerosol Science & Technology* 43 (7):673–8. doi:10.1080/02786820902832960

Maricq, M. M., D. H. Podsiadlik, and R. E. Chase. 2000. Size distributions of motor vehicle exhaust PM: A comparison between ELPI and SMPS measurements. *Aerosol Science and Technology* 33 (3):239–60. doi:10.1080/027868200416231

Maricq, M. M. 2008. Bipolar diffusion charging of soot aggregates. *Aerosol Science & Technology* 42 (4):247–54. doi:10.1080/02786820801958775

Markowicz, P., J. Löndahl, A. Wierzbicka, R. Suleiman, A. Shihadeh, and L. Larsson. 2014. A study on particles and some microbial markers in waterpipe tobacco smoke. *Science of the Total Environment* 499:107–13. doi:10.1016/j.scitotenv.2014.08.055

McMurry, P. H., X. Wang, K. Park, and K. Ehara. 2002. The relationship between mass and mobility for atmospheric particles: A new technique for measuring particle density. *Aerosol Science & Technology* 36 (2):227–38. doi:10.1080/027868202753504083

Mikhailov, E., S. Vlasenko, R. Niessner, and U. Pöschl. 2004. Interaction of aerosol particles composed of protein and saltswith water vapor: Hygroscopic growth and microstructural rearrangement. *Atmospheric Chemistry & Physics* 4 (2):323–50. doi:10.5194/acp-4-323-2004

Mikhailov, E., S. Vlasenko, D. Rose, and U. Pöschl. 2013. Mass-based hygroscopicity parameter interaction model and measurement of atmospheric aerosol water uptake. *Atmospheric Chemistry & Physics* 13 (2):717–40. doi:10.5194/acp-13-717-2013

Montgomery, J. F., S. I. Green, and S. N. Rogak. 2015. Impact of relative humidity on HVAC filters loaded with hygroscopic and non-hygroscopic particles. *Aerosol Science & Technology* 49 (5):322–31. doi:10.1080/02786826.2015.1026433

Mönkkönen, P., I. K. Koponen, K. E. J. Lehtinen, K. Hämeri, R. Uma, and M. Kulmala. 2005. Measurements in a highly polluted Asian mega city: Observations of aerosol number size distribution, modal parameters and nucleation events. *Atmospheric Chemistry & Physics* 5 (1):57–66. doi:10.5194/acp-5-57-2005

Nakao, S., P. Tang, X. Tang, C. H. Clark, L. Qi, E. Seo, A. Asa-Awuku, and D. Cocker. III. 2013. Density and elemental ratios of secondary organic aerosol: Application of a density prediction method. *Atmospheric Environment* 68:273–7. doi:10.1016/j.atmosenv.2012.11.006

Neusüß, C., H. Wex, W. Birmili, A. Wiedensohler, C. Koziar, B. Busch, E. Brüggemann, T. Gnauk, M. Ebert, and D. S. Covert. 2002. Characterization and parameterization of atmospheric particle number-, mass-, and chemical-size distributions in central Europe during LACE 98 and MINT. *Journal of Geophysical Research: Atmospheres* 107 (21):1–13.

Oh, H., H. Park, and S. Kim. 2004. Effects of particle shape on the unipolar diffusion charging of nonspherical particles. *Aerosol Science & Technology* 38 (11):1045–53. doi:10.1080/027868290883324

Olfert, J. S., and N. Collings. 2005. New method for particle mass classification – The Couette centrifugal particle mass analyzer. *Journal of Aerosol Science* 36 (11):1338–52. doi:10.1016/j.jaerosci.2005.03.006

Olfert, J. S., J. P. R. Symonds, and N. Collings. 2007. The effective density and fractal dimension of particles emitted from a light-duty diesel vehicle with a diesel oxidation catalyst. *Journal of Aerosol Science* 38 (1):69–82. doi:10.1016/j.jaerosci.2006.10.002

Ouf, F.-X., and P. Sillon. 2009. Charging efficiency of the electrical low pressure impactor's corona charger: Influence of the fractal morphology of nanoparticle aggregates and uncertainty analysis of experimental results. *Aerosol Science & Technology* 43 (7):685–98. doi:10.1080/02786820902878245

Pagels, J., A. F. Khalizov, P. H. McMurry, and R. Y. Zhang. 2009. Processing of soot by controlled sulphuric acid and water condensation mass and mobility relationship. *Aerosol Science & Technology* 43 (7):629–40. doi:10.1080/02786820902810685

Park, K., F. Cao, D. B. Kittelson, and P. H. McMurry. 2003. Relationship between particle mass and mobility for diesel exhaust particles. *Environmental Science & Technology* 37 (3):577–83. doi:10.1021/es025960v

Peng, J. F., M. Hu, Z. B. Wang, X. F. Huang, P. Kumar, Z. J. Wu, S. Guo, D. L. Yue, D. J. Shang, Z. Zheng, et al. 2014. Submicron aerosols at thirteen diversified sites in China: Size distribution, new particle formation and corresponding contribution to cloud condensation nuclei production. *Atmospheric Chemistry & Physics* 14 (18):10249–65. doi:10.5194/acp-14-10249-2014

Pich, J. 1972. Theory of gravitational deposition of particles from laminar flows in channels. *Journal of Aerosol Science* 3 (5):351–61. doi:10.1016/0021-8502(72)90090-0

Poon, W. S., and B. Y. H. Liu. 1997. Dust loading behavior of engine and general purpose air cleaning filters. *SAE Technical Paper*, 970676.

Pöschl, U. 2005. Atmospheric aerosols: Composition, transformation, climate and health effects. *Angewandte Chemie International Edition* 44 (46):7520–40. doi:10.1002/anie.200501122

Qiao, K., Z. Wu, X. Pei, Q. Liu, D. Shang, J. Zheng, Z. Du, W. Zhu, Y. Wu, S. Lou, et al. 2018. Size-resolved effective density of submicron particles during summertime in the rural atmosphere of Beijing, China. *Journal of Environmental Sciences* 73:69–77. (February). doi:10.1016/j.jes.2018.01.012

Rawat, V. K., D. T. Buckley, S. Kimoto, M. H. Lee, N. Fukushima, and C. J. Hogan. 2016. Two dimensional size-mass distribution function inversion from differential mobility analyzer-aerosol particle mass analyzer (DMA-APM) measurements. *Journal of Aerosol Science* 92:70–82. doi:10.1016/j.jaerosci.2015.11.001

Rissler, J., M. E. Messing, A. I. Malik, P. T. Nilsson, E. Z. Nordin, M. Bohgard, M. Sanati, and J. H. Pagels. 2013. Effective density characterization of soot agglomerates from various sources and comparison to aggregation theory. *Aerosol Science & Technology* 47 (7):792–805. doi:10.1080/02786826.2013.791381

Rissler, J., E. Z. Nordin, A. C. Eriksson, P. T. Nilsson, M. Frosch, M. K. Sporre, A. Wierzbicka, B. Svenningsson, J. Löndahl, M. E. Messing, et al. 2014. Effective density and mixing state of aerosol particles in a near-traffic urban environment. *Environmental Science & Technology* 48 (11):6300–8. doi:10.1021/es5000353

Seinfeld, J. H., and S. N. Pandis. 2012. *Atmospheric chemistry and physics: From air pollution to climate change*. Hoboken: John Wiley & Sons.

Sgro, L. A., A. C. Barone, M. Commodo, A. D'Alessio, A. De Filippo, G. Lanzuolo, and P. Minutolo. 2009. Measurement of nanoparticles of organic carbon in non-sooting flame conditions. *Proceedings of the Combustion Institute* 32 (1):689–96. doi:10.1016/j.proci.2008.06.216

Sgro, L. A., A. De Filippo, G. Lanzuolo, and A. D'Alessio. 2007. Characterization of nanoparticles of organic carbon (NOC) produced in rich premixed flames by differential mobility analysis. *Proceedings of the Combustion Institute* 31 (1):631–8. doi:10.1016/j.proci.2006.08.026

Shin, W. G., G. W. Mulholland, S. C. Kim, J. Wang, M. S. Emery, and D. Y. H. Pui. 2009. Friction coefficient and mass of silver agglomerates in the transition regime. *Journal of Aerosol Science* 40 (7):573–87. doi:10.1016/j.jaerosci.2009.02.006

Shin, W. G., G. W. Mulholland, and D. Y. H. Pui. 2010a. Determination of volume, scaling exponents, and particle alignment of nanoparticle agglomerates using tandem differential mobility analyzers. *Journal of Aerosol Science* 41 (7):665–81. doi:10.1016/j.jaerosci.2010.04.009

Shin, W. G., J. Wang, M. Mertler, B. Sachweh, H. Fissan, and D. Y. H. Pui. 2010b. The effect of particle morphology on unipolar diffusion charging of nanoparticle agglomerates in the transition regime. *Journal of Aerosol Science* 41 (11):975–86. doi:10.1016/j.jaerosci.2010.07.004

Stephens, B., A. Novoselac, and J. A. Siegel. 2010. The effects of filtration on pressure drop and energy consumption in residential HVAC systems (RP-1299). *HVAC&R Research* 16 (3):273–94. doi:10.1080/10789669.2010.10390905

Stephens, B. 2018. Evaluating the sensitivity of the mass-based particle removal calculations for HVAC filters in ISO 16890 to assumptions for aerosol distributions. *Atmosphere* 9 (3):85. doi:10.3390/atmos9030085

Tang, I. N. 1996. Chemical and size effects of hygroscopic aerosols on light scattering coefficients. *Journal of Geophysical Research: Atmospheres* 101 (D14):19245–50. doi:10.1029/96JD03003

Thomas, D., P. Contal, V. Renaudin, P. Penicot, D. Leclerc, and J. Vendel. 1999. Modelling pressure drop in HEPA filters during dynamic filtration. *Journal of Aerosol Science* 30 (2):235–46. doi:10.1016/S0021-8502(98)00036-6

Thomas, D., P. Penicot, P. Contal, D. Leclerc, and J. Vendel. 2001. Clogging of fibrous filters by solid aerosol particles: Experimental and modelling study. *Chemical Engineering Science* 56 (11):3549–61. doi:10.1016/S0009-2509(01)00041-0

Tronville, P., and R. D. Rivers. 2005. International standards: Filters for vehicular applications. *Filtration & Separation* 42 (7):39–43. doi:10.1016/S0015-1882(05)70623-6

Tronville, P., and R. D. Rivers. 2006. Global standards for filter testing. *ASHRAE Journal* 48 (8):58–62.

Valmari, T., M. Lehtimäki, and A. Taipale. 2006. Filter clogging by bimodal aerosol. *Aerosol Science & Technology* 40 (4):255–60. doi:10.1080/02786820500543282

Vijayakumar, R., and K. T. Whitby. 1984. Flat flame ultrafine aerosol generator. *Aerosol Science & Technology* 3 (1):17–24. doi:10.1080/02786828408958989

Vu, T. V., J. Ondracek, V. Zdímal, J. Schwarz, J. M. Delgado-Saborit, and R. M. Harrison. 2017. Physical properties and lung deposition of particles emitted from five major indoor sources. *Air Quality, Atmosphere & Health* 10 (1):1–14. doi:10.1007/s11869-016-0424-1

Wang, H. 2011. Formation of nascent soot and other condensed-phase materials in flames. *Proceedings of the Combustion Institute* 33 (1):41–67. doi:10.1016/j.proci.2010.09.009

Wang, Z., S. M. King, E. Freney, T. Rosenoern, M. L. Smith, Q. Chen, M. Kuwata, E. R. Lewis, U. Pöschl, W. Wang, et al. 2010. The dynamic shape factor of sodium chloride nanoparticles as regulated by drying rate. *Aerosol Science & Technology* 44 (11):939–53. doi:10.1080/02786826.2010.503204

Wang, C., and Y. Otani. 2012. Removal of nanoparticles from gas streams by fibrous filters: A review. *Industrial & Engineering Chemistry Research* 52:5–17. doi:10.1021/ie300574m

Wang, J. 2013. Effects of particle size and morphology on filtration of airborne nanoparticles. *KONA Powder & Particle Journal* 30:256–66. doi:10.14356/kona.2013024

Wang, J., and P. Tronville. 2014. Toward standardized test methods to determine the effectiveness of filtration media against airborne nanoparticles. *Journal of Nanoparticle Research* 16 (6):2417. doi:10.1007/s11051-014-2417-z

Xiao, S., M. Y. Wang, L. Yao, M. Kulmala, B. Zhou, X. Yang, J. M. Chen, D. F. Wang, Q. Y. Fu, D. R. Worsnop, et al. 2015. Strong atmospheric new particle formation in winter in urban Shanghai, China. *Atmospheric Chemistry & Physics* 15 (4):1769–81. doi:10.5194/acp-15-1769-2015

Xie, Y., X. Ye, Z. Ma, Y. Tao, R. Wang, C. Zhang, X. Yang, J. Chen, and H. Chen. 2017. Insight into winter haze formation mechanisms based on aerosol hygroscopicity and effective density measurements. *Atmospheric Chemistry & Physics* 17 (11):7277–90. doi:10.5194/acp-17-7277-2017

Xue, H., A. F. Khalizov, L. Wang, J. Zheng, and R. Zhang. 2009. Effects of coating of dicarboxylic acids on the mass-mobility relationship of soot particles. *Environmental Science & Technology* 43 (8):2787–92. doi:10.1021/es803287v

Yin, Z., X. Ye, S. Jiang, Y. Tao, Y. Shi, X. Yang, and J. Chen. 2015. Size-resolved effective density of urban aerosols in Shanghai. *Atmospheric Environment* 100:133–40. doi:10.1016/j.atmosenv.2014.10.055

Zaatari, M., A. Novoselac, and J. A. Siegel. 2014. The relationship between filter pressure drop, indoor air quality, and energy consumption in rooftop HVAC units. *Building & Environment* 73:151–61.

Zelenyuk, A., Y. Cai, and D. Imre. 2006. From agglomerates of spheres to irregularly shaped particles: Determination of dynamic shape factors from measurements of mobility and vacuum aerodynamic diameters. *Aerosol Science & Technology* 40 (3):197–217. doi:10.1080/02786820500529406

Zelenyuk, A., J. Yang, C. Song, R. A. Zaveri, and D. Imre. 2008. A new real-time method for determining particles' sphericity and density: Application to secondary organic aerosol formed by ozonolysis of α-pinene. *Environmental Science & Technology* 42 (21):8033–8. doi:10.1021/es8013562

Zhang, Z., and F. Jiang. 2016. In-place HEPA filter testing by the sodium flame method. *Powder Technology* 301:615–21. doi:10.1016/j.powtec.2016.06.046